Ultramicroscopy 195 (2018) 171–188

Contents lists available at ScienceDirect

Ultramicroscopy

journal homepage: www.elsevier.com/locate/ultramic

A *single slice* approach for simulating two-beam electron diffraction of nanocrystals

Lionel Cervera Gontard[a,b,*], Adrián Barroso-Bogeat[b], Rafal E. Dunin-Borkowski[c], José Juan Calvino[b]

[a] Departamento de Ciencia de los Materiales e Ingeniería Metalúrgica y Química Inorgánica, Universidad de Cádiz, Puerto Real 11510, Spain
[b] Departamento de Ingeniería Informática, Universidad de Cádiz, Puerto Real 11510, Cádiz, Spain
[c] Ernst Ruska-Centre for Microscopy and Spectroscopy with Electrons and Peter Grünberg Institute, Forschungszentrum Jülich, 52425 Jülich, Germany

ARTICLE INFO

Keywords:
Electron diffraction simulation
Shape factor
Dynamical diffraction
Electron precession

ABSTRACT

A simple computational method that can be used to simulate TEM image contrast of an electron beam diffracted by a crystal under two-beam dynamical scattering conditions is presented. The approach based on slicing the shape factor is valid for a general crystal morphology, with and without crystalline defects, avoids the column approximation, and provides the complex exit wave at the focal and the image planes also under weak-beam conditions. The approach is particularly efficient for large crystals and the 3D model required for the calculations can be measured experimentally using electron tomography. The method is applied to show that the shape of a diffracted spot can be affected by shifts, broadening and secondary maxima of appreciable intensity, even for a perfect crystal. The methodology is extended for the case of electron precession diffraction, and to show how can be used to improve nanometrology from diffraction patterns. The method is used also to perform simulations of simple models of crystalline defects. The accuracy of the method is demonstrated through examples of experimental and simulated dark-field images of MgO and ZrO_2 nanocrystals and thin layers of CeO_2.

1. Introduction

Transmission electron microscopy (TEM) is widely used to provide important information about the crystalline structures of materials using imaging and diffraction. Real space information is obtained by recording the intensity $I(x, y)$ at points in the image plane of the objective lens, while reciprocal space information is obtained by recording the intensity $I(q_x, q_y)$ in a diffraction pattern formed in the focal plane of the objective lens [1–3]. Images acquired using conventional TEM (bright-field (BF) and dark-field (DF) modes) are directly interpretable when used for studying amorphous specimens in which the contrast is dominated by mass-thickness contrast. However, when studying crystalline materials, dynamical scattering complicates the interpretation of recorded intensities.

Different theories and algorithms have been proposed to predict and understand TEM images and diffraction patterns, including solutions to full dynamical many-beam calculations using Bloch wave methods for perfect crystals, exit wave reconstruction and multislice methods for general crystals. These approaches can be used to calculate the complex exit surface wave function at atomic resolution, and hence, the diffraction pattern [4–7]. However, Bloch wave methods can only be used for perfect crystals and exit wave restoration methods are demanding regarding the acquisition of experimental data. A difficulty of multislice methods is that of choosing the right slice thickness for general orientations of the crystal. And they can be computationally demanding for simulating large nanocrystals, as they require atomistic models (which may contain thousands of atoms even for small crystals) and a full recalculation of the propagation of the electron wave is needed each time certain parameters (e.g., the sample or beam tilt) are changed. An alternative simpler low-resolution method of simulating BF and DF images is based on the solution of the Howie–Whelan differential equations in their two-beam form [1,8]. Image contrast features (in two-beam mode) are qualitatively the same at all acceleration voltages and independent of the crystal structure. These equations provide a complex solution but are typically solved for simulating the image intensities with the so-called “column approximation”, and in some situations they can fail to reproduce image details of defects or even of perfect crystals under weak-beam conditions [9,10]. Alternatively, in the kinematical approximation, the fine structure of the image intensities of a diffraction spot recorded from a crystal has been simulated in a simple manner by slicing the shape factor [11]. This approach has involved the formulation of analytical solutions to

* Corresponding author.
E-mail address: lionel.cervera@uca.es (L.C. Gontard).

https://doi.org/10.1016/j.ultramic.2018.09.004
Received 24 May 2018; Received in revised form 31 August 2018; Accepted 12 September 2018
Available online 13 September 2018

describe the shapes of specific nanocrystal geometries [11–14].

Here, we present a numerical method, the 'single slice approach', which can be used to efficiently generate simulations of two-beam dynamical complex amplitudes of diffracted spots in the focal and image planes of an electron microscope. We describe the theoretical framework of the method and we introduce the concept of the *g*-shape function that can be used to model defects in crystals within the 'single slice' framework. And we evaluate the accuracy of the method by comparing simulations with experimental images of different crystalline materials.

2. Methods and results

2.1. Slicing the kinematical shape factor

Within the framework of kinematical diffraction theory, the complex amplitude of a diffracted beam ϕ_g scattered in the direction $\boldsymbol{k}' = \boldsymbol{k} + \boldsymbol{g} + \boldsymbol{q}$ at distance r is given by the expression

$$\phi_g(\boldsymbol{q}) = \frac{1}{r}\frac{F_g}{V_c} \iiint \exp[-2\pi i(\boldsymbol{q}\cdot\boldsymbol{r})d\boldsymbol{r}] \tag{1}$$

where V_c is the volume of the unit cell, F_g is the structure factor, a real constant of the unit cell when absorption is not considered for the reflection corresponding to the reciprocal vector $\boldsymbol{g}$, $\boldsymbol{k}$ is the incident electron beam direction and $\boldsymbol{q} = (q_x,\ q_y,\ q_z)$ is a reciprocal lattice vector, whose origin is at the reciprocal lattice point $\boldsymbol{g}$. The integral in Eq. (1) is, by definition, the three-dimensional Fourier transform of an oriented crystal, whose shape in real space can be defined by the function $\mathcal{D}(\boldsymbol{r}) = \mathcal{D}(x, y, z)$, which takes a value of unity inside the crystal and zero outside it.

$$\mathcal{D}(\boldsymbol{r}) = \begin{cases} \textit{perfect crystal} \rightarrow 1 \\ \textit{outside the crystal} \rightarrow 0 \end{cases}$$

Eq. (1) can therefore be written as a product in the form

$$\phi_g(\boldsymbol{q}) = \frac{1}{r}\frac{F_g}{V_c}\mathcal{FT}_{3D}\{\mathcal{D}(\boldsymbol{r})\} \equiv \frac{1}{r}\frac{F_g}{V_c}D(\boldsymbol{q}), \tag{2}$$

where $D(\boldsymbol{q})$ is referred to as the shape transform and is a complex quantity. In the kinematical approximation, which is often valid for X-rays and for small crystals in weakly diffracting orientations for electrons, each reciprocal lattice spot is convoluted with the function $D(\boldsymbol{q})$, whose spatial orientation is linked to that of the crystal (Fig. 1a). For example, for a thin crystalline slab, each reciprocal lattice spot is elongated in a direction parallel to the shortest dimension of the crystal. Fig. 1b shows examples of crystal shape (for a cuboctahedron, a disc and an octahedron) and corresponding shape factor (i.e., the modulus squared of the shape transform) $|D(\boldsymbol{q})|^2$.

According to Eq. (2), the fine structure of a diffraction spot from a nanocrystal depends on its morphology and crystallographic structure, on the atomic species present and on the orientation of the crystal and the direction, shape and wavelength of the electron beam. In this context, it is convenient to refer to the Ewald sphere geometrical interpretation of diffraction. A plane electron beam of wavelength λ that illuminates a crystal can be represented in reciprocal space by a sphere of radius $1/\lambda$. It is only when the shape factor that is associated with each reciprocal lattice spot is intersected by the Ewald sphere that the corresponding beam will diffract (Fig. 1a). Typically, in electron diffraction many reciprocal points may be crossed by the Ewald sphere and correspondingly many beams may be excited at any time. When the electron beam is tilted by an angle $\Delta\theta$, the Ewald sphere rotates by angle $\Delta\theta$ around a point on the circumference of the sphere; if the sample is rotated by an angle $\Delta\theta$, then the sphere is fixed and the reciprocal lattice points rotate by an angle $\Delta\theta$. Because of the high energy of the incident electron beam, the Ewald sphere can be approximated locally as a plane. Moreover, because $\boldsymbol{k}' \cong \boldsymbol{k}$, the plane is approximately perpendicular to the electron beam direction at each reflection and intersects the shape factor at a distance $q_z = s_g$, which is referred to as the deviation parameter (Fig. 1b). For example, the technique of coherent diffraction tomography uses a tilted series of diffraction patterns to rebuild the three-dimensional shape factor [15]. In general, s_g is different for each reflection $\boldsymbol{g}$ and is given by the expression $s_g = |\boldsymbol{g}|\ \Delta\theta$. If we use the Ewald sphere interpretation to Eq. (2) the complex amplitude ϕ_g of a scattered beam $\boldsymbol{g}$ is then described by a cross-section of the kinematical shape factor in the form

$$\phi_g(q_x, q_y) = \frac{1}{r}\frac{F_g}{V_c} D(q_x, q_y;\ q_z = s_g) \cong \frac{F_g}{V_c} D(s_g), \tag{3}$$

where the factor $1/r$ has been dropped in the rightmost term because the Bragg scattered wave is close to being planar at large distances r compared with the unit cell dimensions (Fraunhofer diffraction).

The complex diffracted amplitude in Eq. (3) depends on the reciprocal space coordinates q_x and q_y, which correspond to the coordinates of the diffraction pattern in the back focal plane of the objective lens. Fig. 1b shows a representation in Fourier space of a shape factor intersected by two possible planar cross-sections at $s_g = 0$ and $s_g \neq 0$. When referred to the origin $\boldsymbol{g}$, points within the slices are defined by the vectors $\boldsymbol{q} = (q_x, q_y, s_g)$. The parameter s_g is fixed experimentally by the tilt of the crystal relative to the incident electron beam. The intensity that is measured on a detector is then given by the expression

$$I_g(q_x, q_y) = \phi_g \cdot \phi_g^* = \left(\frac{F_g}{V_c}\right)^2 |D(s_g)|^2. \tag{4}$$

Note that Eq. (3) does not describe the atomic potential within the unit cell but only the variations of the crystal shape from unit cell to unit cell. The phase obtained of the Fourier component in reciprocal space using Eq. (3) is a "crystalline phase", linked to description of the shape of the crystal [16].

2.2. Slicing the kinematical shape factor and the column approximation

According to the Howie-Whelan equations, under two-beam kinematical conditions the intensity diffracted from a thin film in the direction $\boldsymbol{k}'$ is given by the expression

$$I_g = |\phi_g|^2 = \frac{\pi^2}{\xi_g^2}\frac{sin^2\ \pi t\ s_g}{(\pi s_g)^2}, \tag{5}$$

where $\xi_g = \pi V_c \cos\theta_B/\lambda F_g \approx \pi V_c/\lambda F_g$ is the extinction distance for reflection $\boldsymbol{g}$ and t is the specimen thickness. Eq. (5) simulates the real space intensity of a thin crystal in the column approximation [10]. Since the scattering angles are small, electron diffraction is essentially a forward scattering process. Therefore, even after being scattered several times, most electrons will travel nearly parallel to the incident electron beam direction. It is then generally assumed that an electron which enters the foil at one point never leaves a cylindrical column centred on that point. The crystal is then divided into columns that lie parallel to the direction $\boldsymbol{k}$ and the image intensity is calculated column-by-column for different local values of specimen thickness, t, and deviation parameter, s_g.

Following a similar derivation given by Humphreys [17] we illustrate next that the Howie-Whelan solution given by Eq. (5) is a particular solution of the "Ewald sphere" approach (of slicing the shape factor) given by Eq. (3).

Consider a thin crystalline slab that has lateral dimensions A x B and thickness t, where A, B $> > t$, according to Eq. (3), the intensity scattered in a direction $\boldsymbol{k}' = \boldsymbol{k} + \boldsymbol{g} + \boldsymbol{q}$ at a large distance r can be obtained slicing the shape factor with a deviation parameter as

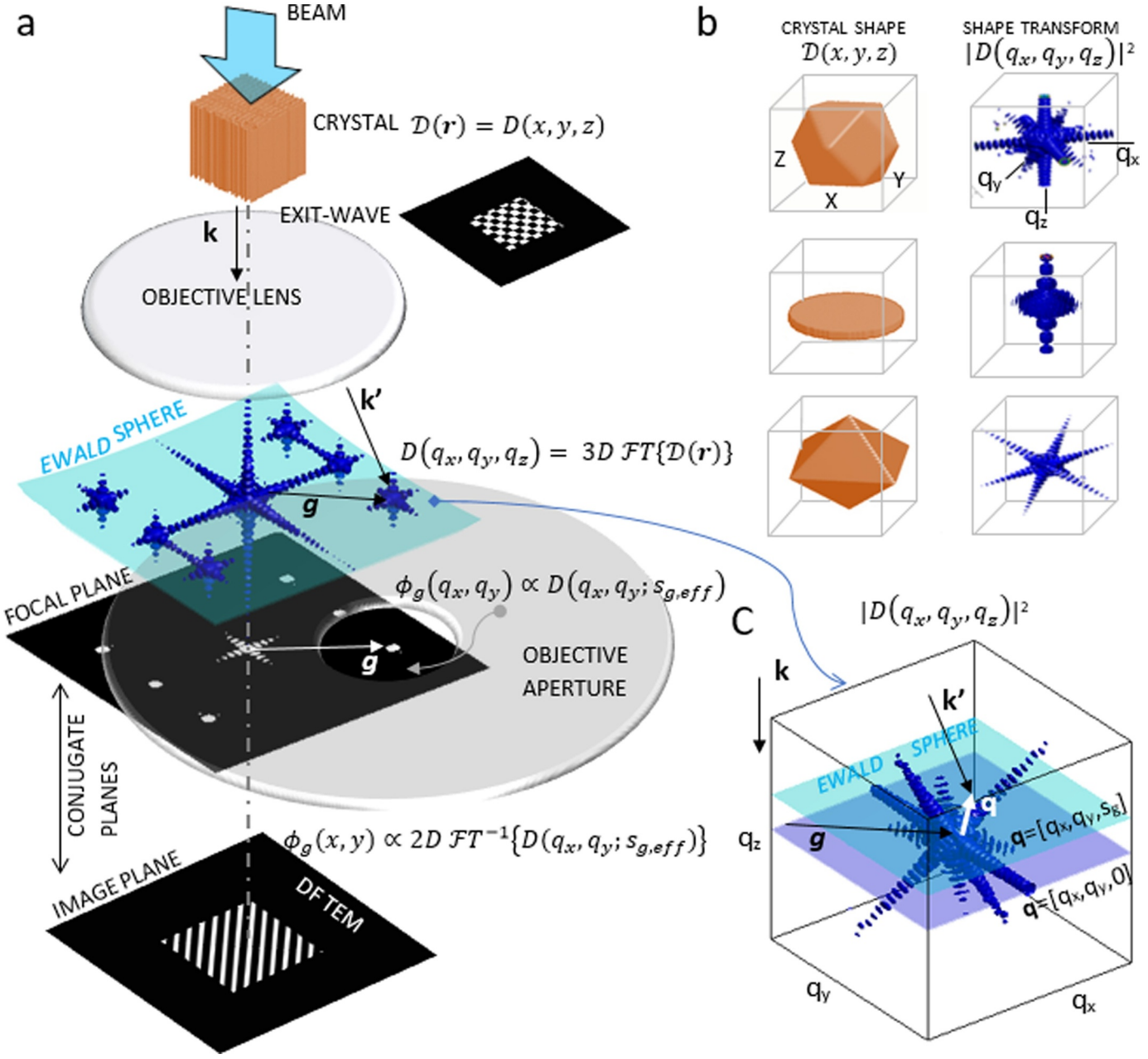

Fig. 1. (a) Schematics of a transmission electron microscope. The diffraction pattern and the image plane of the objective lens are conjugated planes. The objective aperture at the focal plane can be used to select only one diffracted beam $\phi_g(q_x, q_y)$, thus forming a DF image. (b) Nanocrystal shapes $\mathcal{D}(x, y, z)$, for a cuboctahedron, a disc and an octahedron and their corresponding shape factors, which are given by the modulus squared of $D(q_x, q_y, q_z)$ in reciprocal space. (c) Detail of the three-dimensional shape factor of one cuboctahedrom in random orientation. The amplitude in the diffraction plane $\phi_g(q_x, q_y)$ corresponds to a planar intersection of the Ewald sphere with the shape factor $D(q_x,\ q_y,\ q_z = s_g)$ at the deviation parameter s_g.

$$I_g(q_x, q_y) = \left(\frac{1}{r}\frac{F_g}{V_c}\right)^2 |D(s_g)|^2 = \left(\frac{1}{r}\frac{F_g}{V_c}\right)^2 \left(\frac{sin\ \pi t s_g}{\pi s_g}\right)^2 \left(\frac{sin\ \pi A q_x}{\pi q_x}\right)^2 \left(\frac{sin\ \pi B q_y}{\pi q_y}\right)^2 . \quad (6)$$

For large values of A and B, the terms that involve A and B tend to δ functions and

$$I_g(q_x, q_y) = \left(\frac{1}{r}\frac{F_g}{V_c}\right)^2 \left(\frac{sin\ \pi t s_g}{\pi s_g}\right)^2 A\ \delta(q_x) B\ \delta(q_y) . \quad (7)$$

If we consider the intensity scattered about the diffracted beam $\boldsymbol{k}' = \boldsymbol{k} + \boldsymbol{g}$ into solid angle $d\Omega$ by an element of area dS of radius r at the exit surface of the crystal then $r^2 d\Omega = dS$. In reciprocal space $d\Omega = dq_x\ dq_y\ \lambda^2/\cos\theta_B$ (where θ_B is the Bragg angle for reflection $\boldsymbol{g}$) and the total intensity scattered over a sphere of radius r about the diffracted beam direction $\boldsymbol{k'}$ is

$$\int I dS = \frac{AB\ F_g^2 \lambda^2}{V_c^2 \cos\theta_B} \left(\frac{sin\ \pi t s_g}{\pi s_g}\right)^2 \int \delta(q_x) dq_x \int \delta(q_y) dq_y . \quad (8)$$

As $AB\cos\theta_B$ is the area of the crystal projected along $\boldsymbol{k'}$ and the integrals are 1, the intensity *per unit area* of the diffracted beam, i.e., the diffracted beam flux, is

$$I_g = \frac{F_g^2 \lambda^2}{V_c^2 \cos\theta_B^2} \left(\frac{sin\ \pi t s_g}{\pi s_g}\right)^2 = \frac{\pi^2}{\xi_g^2} \left(\frac{sin\ \pi t s_g}{\pi s_g}\right)^2 . \quad (9)$$

Summarising, slicing the shape factor using Eq. (3) (or (4)) is a valid approach for calculating electron diffraction under kinematical conditions, and it does not require the column approximation. The classical Howie-Whelan two-beam solution Eqs. (9) or ((5)) is recovered as a particular solution of Eq. (3) when an infinite crystal with finite thickness is considered.

2.3. Simulation of the fine structure of two-beam dynamical diffraction

2.3.1. Diffracted spots

Although the kinematical theory of diffraction provides a useful qualitative guide to the interpretation of transmission electron micrographs of crystals, it is valid only when the amplitude ϕ_g of the diffracted wave is small in comparison with that of the incident wave ϕ_o. If the amplitude of the diffracted wave becomes large, then it can be scattered again. For crystals, whose thickness is comparable to or greater than ξ_g, the kinematical approximation is usually not valid and dynamical theory must be used [8,9]. The dynamical intensity of a diffracted beam $\boldsymbol{g}$ in a two-beam condition is given by the expression

$$I_g = |\phi_g|^2 = \frac{\pi^2}{\xi_g^2}\,\frac{sin^2\ \pi t s_{g,eff}}{(\pi s_{g,eff})^2}, \tag{10}$$

or the Howie-Whelan two-beam solution under dynamical conditions. This equation has exactly the same form as that for the kinematical intensity in Eqs. (5) and (9). The only difference being that s_g is replaced by the "effective" deviation parameter

$$s_{g,eff} = \sqrt{s_g^2 + \frac{1}{\xi_g^2}}\ . \tag{11}$$

Just as we did for the kinematical case, we reinterpret Eq. (10) as being an approximation of the more general Eq. (4), in which the kinematical shape factor $D(\boldsymbol{q})$, now under dynamical conditions, is sliced at an effective distance $s_{g,\ eff}$ instead of s_g, using the expression

$$s_{g,eff} = sign(s_g)\ \times \sqrt{s_g^2 + \frac{1}{\xi_g^2}}\ . \tag{12}$$

Then, the amplitude of a diffracted beam ϕ_g scattered under dynamical two-beam conditions in the direction $\boldsymbol{k}' = \boldsymbol{k} + \boldsymbol{g} + \boldsymbol{q}$ is

$$\phi_g(q_x, q_y) = \frac{F_g}{V_c}\,D(q_x, q_y; q_z = s_{g,eff}) \equiv \frac{F_g}{V_c}\,D(s_{g,eff})\ . \tag{13}$$

And the *diffracted* intensity in the focal plane of the objective lens is therefore identical to that in a planar slice of the kinematic shape factor at a distance $q_z = s_{g,eff}$, given by the expression

$$I_g(q_x, q_y) = \phi_g \cdot \phi_g^* = \left(\frac{F_g}{V_c}\right)^2 |D(q_x, q_y; s_{g,eff})|^2 \equiv \left(\frac{F_g}{V_c}\right)^2 |D(s_{g,eff})|^2. \tag{14}$$

Fig. 2b shows the kinematical shape factor $D(q_x, q_z)$ of a bi-dimensional crystal with square shape $D(x, z)$ shown in Fig. 2a. The "dynamical" shape factor shown in Fig. 2d is obtained by restacking slices from $D(q_x, s_g)$ to $D(q_x, s_{g,eff})$ using Eq. (11). The gap in Fig. 2c and d exists when the scattering is dynamical and the deviation parameter $|s_g| \geq 1/\xi_g$.[1]

2.3.2. Precession electron diffraction

Precession electron diffraction, PED [18] is a technique that permits the acquisition of quasi-kinematical electron diffraction patterns and provides a powerful approach for the *ab initio* solution of crystal structures. Eq. (14) can be used to simulate the influence of electron precession on a diffraction pattern. The technique relies on tilting the incident electron beam by an angle Φ and precessing the beam about the optical axis of the microscope. The diffraction pattern is measured over a much longer acquisition time than the period of precession. With reference to the Ewald sphere interpretation of diffraction, the measurement corresponds to not a single slice of the shape factor but an incoherent sum of *2* slices with deviation parameters of $s_g^i = [-g\frac{\Phi}{2},\ -g\frac{\Phi}{2}]$ given by the expression

$$I_{g,precession}(q_x, q_y) = \left(\frac{F_g}{V_c}\right)^2 \sum_i |D(q_x, q_y; s_g^i)|^2 \equiv \left(\frac{F_g}{V_c}\right)^2 \sum_i |D(s_g^i)|^2 \tag{15}$$

2.3.3. Simulation of dark-field TEM images

The image plane and the focal plane (Fraunhoffer diffraction) in the electron microscope are Fourier conjugate planes, and the objective lens of the microscope effectively performs a Fourier transform between both planes (Fig. 1a). Therefore, the complex amplitude in the image plane for a reflection $\boldsymbol{g}$, $\phi_g(x, y)$, can be calculated by taking the two-dimensional Fourier transform of a planar slice of the complex amplitude $\phi_g(q_x, q_y)$ at a distance $q_z = s_{g,eff}$ given by the expression,

$$\phi_g(x, y) = \mathcal{FT}^{-1}\{\phi_g(q_x, q_y; s_{g,eff})\}. \tag{16}$$

And the diffracted intensity in the image plane of the objective lens will be

$$\begin{aligned} I_g(x, y) &= |\phi_g(x, y)|^2 = |\mathcal{FT}^{-1}\{\phi_g(q_x, q_y; s_{g,eff})\}|^2 \\ &= \left(\frac{F_g}{V_c}\right)^2 \cdot |\mathcal{FT}^{-1}\{D(q_x, q_y; s_{g,eff})\}|^2. \end{aligned} \tag{17}$$

2.2.4. Simulation at the image and focal planes including absorption

A more accurate simulation of the images must take into account that the intensity does not remain localized in the Bragg reflection. The diffuse electron scattering between the Bragg diffraction spots by inelastic and thermal diffuse scattering causes a decrease of intensity in the Bragg spots themselves [19]. If anomalous absorption produces an asymmetry between the bright field intensities for positive and negative excitation errors for dark field intensity simulation only normal absorption must be considered [2,20,21] which has the effect of attenuating the intensities with increasing thickness of the crystal. Normal absorption can be modelled at the image plane by adding an exponential factor to the image intensity,

$$I_g(x, y) = \left(\frac{F_g}{V_c}\right)^2 \cdot |\mathcal{FT}^{-1}\{D(q_x, q_y;\ s_{g,eff})\}|^2 \cdot e^{\frac{-2\pi}{\xi'_o} z(x,y)}, \tag{18}$$

where $z(x, y)$ is the projected thickness of the crystal taken along the z-direction, the direction of the incoming electron beam, and ξ'_o is a real value proportional to the extinction distance, ξ_g. The function $z(x, y)$ can be calculated numerically integrating the function $\mathscr{D}(\boldsymbol{r}) = \mathscr{D}(x,\ y,\ z)$ along z, or alternatively, by slicing the calculated shape factor, $D(\boldsymbol{q})$, at $q_z = 0$,

$$z(x, y) = |\mathcal{FT}^{-1}\{D(q_x, q_y, q_z = 0)\}| \equiv |\mathcal{FT}^{-1}\{D(0)\}|, \tag{19}$$

for which we have taken into account the equivalence stated by the *Central Slice Theorem* (see Supporting information).

Combining the Eqs. (18) and (19) the two-beam dynamical image intensity in the image plane for a reflection $\boldsymbol{g}$ including normal absorption is

$$I_g(x, y) = \left(\frac{F_g}{V_c}\right)^2 \cdot |\mathcal{FT}^{-1}\{D(q_x, q_y; s_{g,eff})\}|^2 \cdot e^{\frac{-2\pi}{\xi'_o} |\mathcal{FT}^{-1}\{D(q_x, q_y; 0)\}|}, \tag{20}$$

and the complex amplitude in the image plane is given by

[1] The meaning of the gap is explained in terms of the Bloch wave formalism. In two-beam conditions the diffracted beam $\boldsymbol{g}$ inside the crystal is a periodic wave with a wavevector of modulus $\Delta k = |\boldsymbol{k}^{(2)} - \boldsymbol{k}^{(1)}|$, which results from the sum of two Bloch waves with wavevectors $\boldsymbol{k}^{(1)}$ and $\boldsymbol{k}^{(2)}$ that interfere. The periodic wave (and the diffracted beam $\boldsymbol{g}$) can exist only when $\Delta k = |s_{g,eff}|$.

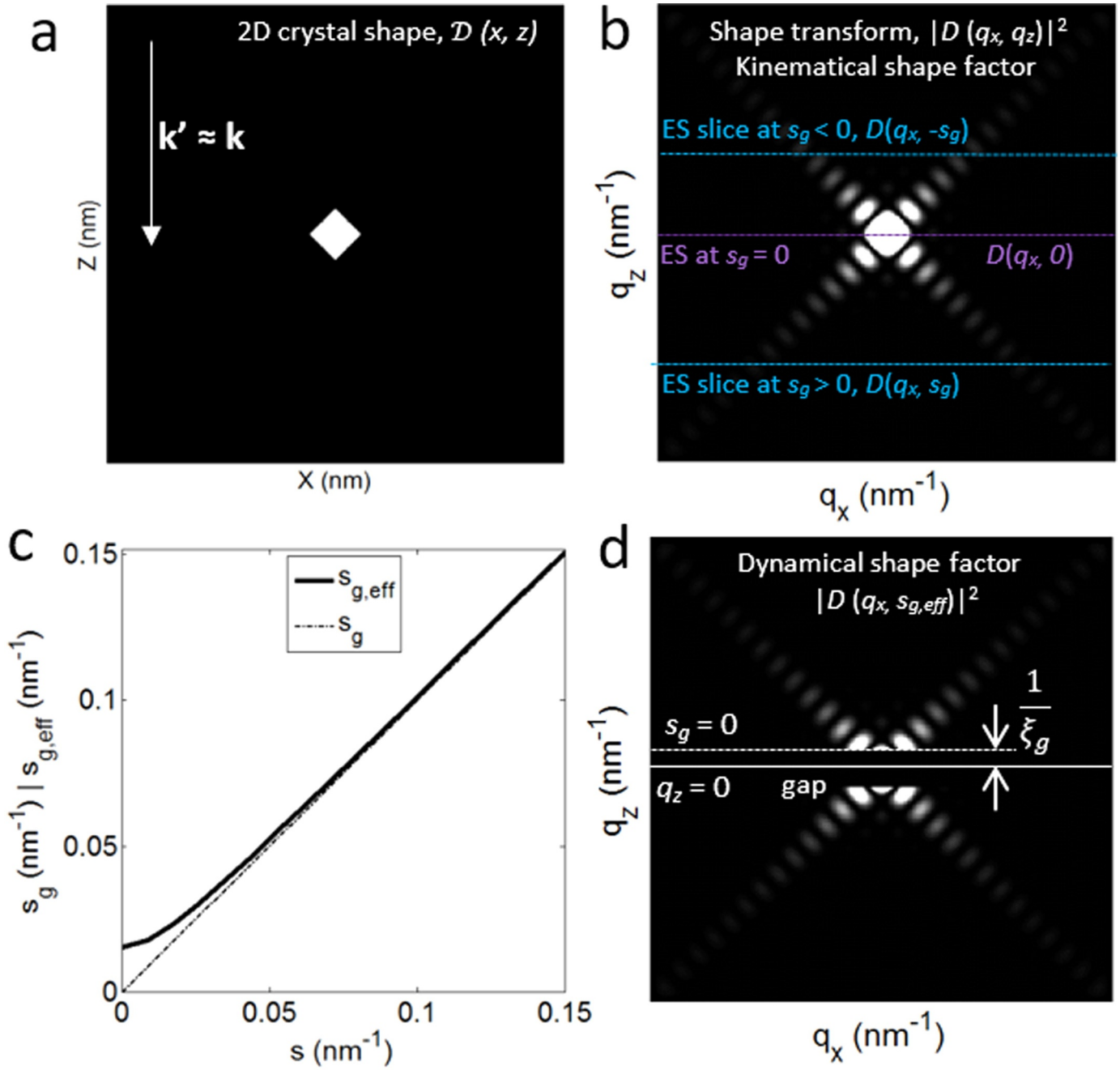

Fig. 2. (a) Two-dimensional crystal with a square shape $\mathcal{D}(x, z)$ and (b) the corresponding kinematical shape factor. The dotted lines represent one-dimensional Ewald sphere (ES) slices through the two-dimensional shape factor for $s_g = 0$ and $s_g \neq 0$. The electron beam direction is from top to bottom. (c) The deviation parameter s_g and the effective deviation parameter $s_{g,eff}$ plotted for the kinematical and dynamical cases using Eq. (11) for $\boldsymbol{g} = (2\ 0\ -2)$, $V_g = 6.688$ V and $\xi_g = 64.988$nm. (d) Effective shape factor calculated by re-stacking slices of the kinematical shape factor using the effective deviation parameter $s_{g,eff}$ using Eq. (13).

$$\phi_g(x, y) = \frac{F_g}{V_c} \cdot \mathcal{FT}^{-1}\{D(q_x, q_y; s_{g,eff})\} \cdot e^{\frac{-\pi}{\xi'_o}|\mathcal{FT}^{-1}\{D(q_x,q_y;0)\}|}. \tag{21}$$

At the focal plane of the objective lens the amplitude $\phi_g(q_x, q_y)$ is the Fourier transform of the amplitude at the image plane (Eq. (21)), or

$$\begin{aligned}\phi_g(q_x, q_y) &= \frac{F_g}{V_c} \cdot \mathcal{FT}\{\mathcal{FT}^{-1}\{D(s_{g,eff})\}\} * \mathcal{FT}\left\{e^{\frac{-\pi}{\xi'_o}|\mathcal{FT}^{-1}\{D(0)\}|}\right\} \\ &= \frac{F_g}{V_c} \cdot D(s_{g,eff}) * \mathcal{FT}\left\{e^{\frac{-\pi}{\xi'_o}|\mathcal{FT}^{-1}\{D(0)\}|}\right\}.\end{aligned} \tag{22}$$

The Fourier transform of the decaying exponential in Eq. (22) has the following transform,

$$FT\left[e^{-\pi k_o x}\right] = \frac{2}{\pi} \frac{k_o}{k_o^2 + q^2}, \tag{23}$$

being k_o a real constant, and Eq. (22) can be written like

$$\begin{aligned}\phi_g(q_x, q_y) &= \frac{F_g}{V_c} \cdot D(q_x, q_y; s_{g,eff}) * \frac{2}{\pi} \cdot \frac{\frac{1}{\xi'_o}}{\left(\frac{1}{\xi'_o}\right)^2 + D(q_x, q_y; 0)^2} \\ &\equiv \frac{F_g}{V_c} \cdot D(s_{g,eff}) * \frac{2}{\pi \xi'_o} \cdot \frac{1}{\left(\frac{1}{\xi'_o}\right)^2 + D(0)^2}.\end{aligned} \tag{24}$$

Then, at the focal plane the amplitude is the convolution (operator *) of one slice of the shape transform with a function of the slice $D(0)$

through the centre (the projected thickness of the crystal). And finally, the intensity in the focal plane including absorption is the modulus squared of Eq. (24),

$$I_g(q_x, q_y) = \left| \frac{F_g}{V_c} \cdot D(s_{g,eff})^* \frac{2}{\pi \xi'_o} \cdot \frac{1}{\left(\frac{1}{\xi'_o}\right)^2 + D(0)^2} \right|^2 . \tag{25}$$

In summary, Eqs. (20) and (25) can be used to simulate the dynamical diffracted intensity in two-beam condition at the focal and image planes of a TEM, including the effect of normal absorption.

2.2.5. The g-shape factor and the simulation of defects

One of the goals of image simulation is understanding the contrast of experimental images of crystalline sample with defects. Images of defects are often acquired experimentally in dark field mode, and they are simulated using the Howie-Whelan equation and the column approximation. However, these fail in some situations like for single points defects. To remedy this, the Howie-Basinski equation set can be used, which avoids the column approximation and gives approximate solutions of the time-independent Schrödinger equations describing high-energy electrons propagating through a crystalline foil containing a defect [9,22].

Here instead, we study the feasibility of the single slice approach for simulating the contrast arising from defects. Firstly, we note that the shape function $\mathcal{D}(\boldsymbol{r})$ used in Eq. (2) was defined as a function that describes the boundaries of a perfect crystal. The shape factor was calculated as the Fourier integral of $\mathcal{D}(\boldsymbol{r})$, a function which contains all of the information of the geometry of the perfect crystal. $\mathcal{D}(\boldsymbol{r})$ is the same for every diffracted beam $\boldsymbol{g}$. The only difference between different reflections is the value of the structure factor of the reflection, which is related to the Fourier component of the electrostatic potential by the expression

$$F_g/V_c = \sigma V_g/\lambda, \tag{26}$$

where σ is the interaction constant ($\sigma = 2\pi me\lambda/h^2$) being m and e the mass and the charge of one electron, and h is the Planck constant. A defect displaces the positions of the unit cells of the perfect crystal, thus, altering the electrostatic scattering potential V_g seen by an electron. The amount of change of V_g is a function of the local distortion of the family of $\boldsymbol{g}$-planes. Therefore, when a defect occurs the shape function, $\mathcal{D}(\boldsymbol{r})$ is no longer the same for every diffracted beam. Instead, in general each set of $\boldsymbol{g}$-planes will have associated a '$\boldsymbol{g}$-shape function', $\mathcal{D}_g(\boldsymbol{r})$ that describes how F_g (or V_g) changes locally with the local displacement $\boldsymbol{R}(\boldsymbol{r})$ of the unit cells, so that the amplitude of a diffracted beam in two-beam condition will be given by

$$\phi_g(\boldsymbol{q}) = \frac{F_g}{V_c} \iiint \mathcal{D}_g(\boldsymbol{r}) \exp[-2\pi i(\boldsymbol{q}\cdot\boldsymbol{r})]\, d\boldsymbol{r} = \frac{F_g}{V_c} D_g(\boldsymbol{q}), \tag{27}$$

The subscript $\boldsymbol{g}$ is added to the shape function (and the shape factor) to indicate that for imperfect crystals the shape function (and the shape factor) will be different for different sets of lattice planes.

We define such a modified g-shape function as follows,

$$\mathcal{D}_g(\boldsymbol{r}) = \begin{cases} \text{undistorted } g \rightarrow 1 \\ \text{outside crystal or at a discontinuity} \rightarrow 0, \\ \text{strain of the g planes} \rightarrow e^{-2\pi i \boldsymbol{g}\cdot\boldsymbol{R}(\boldsymbol{r})} \end{cases} \tag{28}$$

where three cases are considered:

(i) $\mathcal{D}_g(\boldsymbol{r})$ is 1 wherever the $\boldsymbol{g}$-set of planes are not distorted (the potential is V_g).
(ii) $\mathcal{D}_g(\boldsymbol{r})$ is zero whenever the periodicity of the $\boldsymbol{g}$-planes is broken, such as at the facets of the crystal, or whenever the crystal planes change direction abruptly, like for example, at a stacking fault.
(iii) Where the $\boldsymbol{g}$-set of planes is strained, the shape function $\mathcal{D}_g(\boldsymbol{r})$ is a complex function that depends on the local displacement field, $\boldsymbol{R}(\boldsymbol{r})$. This is a well-known result of diffraction theory of defects [1–3] that models the effect of local strain as a phase change given by $e^{-2\pi i \boldsymbol{g}\cdot\boldsymbol{R}(\boldsymbol{r})}$, and the problem of calculating Eq. (27) reduces to finding the scalar product $\boldsymbol{g}\cdot\boldsymbol{R}(\boldsymbol{r})$.

If $\mathcal{D}_g(\boldsymbol{r})$ Eq. (28) is known or can be calculated, the two-beam dynamical diffracted amplitude and intensity can be simulated in the focal and image planes as in the case of a perfect crystal by single slicing the $\boldsymbol{g}$-shape factor $D_g(\boldsymbol{q}) = D_g(q_x, q_y, q_z)$. The intensity in the focal plane is then given by the expression

$$\begin{aligned} I_g(q_x, q_y) &= \left(\frac{F_g}{V_c}\right)^2 |D_g(\boldsymbol{q}; s_{g,eff})|^2 = \left(\frac{F_g}{V_c}\right)^2 |D_g(q_x, q_y; s_{g,eff})|^2 \\ &\equiv \left(\frac{F_g}{V_c}\right)^2 |D_g(s_{g,eff})|^2, \end{aligned} \tag{29}$$

and the intensity in the image plane is

$$I_g(x, y) = \left(\frac{F_g}{V_c}\right)^2 \cdot |\mathcal{F}T^{-1}\{D_g(s_{g,eff})\}|^2. \tag{30}$$

And if normal absorption is included, the intensities in the focal and image plane are respectively

$$I_g(q_x, q_y) = \left| \frac{F_g}{V_c} \cdot D_g(s_{g,eff})^* \frac{2}{\pi \xi'_o} \cdot \frac{1}{\left(\frac{1}{\xi'_o}\right)^2 + D(0)^2} \right|^2 , \tag{31}$$

and

$$I_g(x, y) = \left(\frac{F_g}{V_c}\right)^2 \cdot |\mathcal{F}T^{-1}\{D_g(s_{g,eff})\}|^2 \cdot e^{\frac{-2\pi}{\xi'_o} z(x,y)}, \tag{32}$$

3. Results

In the following sections we apply the single slicing approach to simulate dark-field electron diffraction contrast in a variety of practical problems. Several of the results can be replicated using the Matlab code provided in the Appendix.

3.1. Simulations of the fine structures of diffracted spots

3.1.1. Diffracted spots of MgO crystals

Fig. 3 illustrates the application of Eq. (14) to the simulation of the diffracted intensities of MgO crystals for different orientations. A sample of MgO smoke crystals was prepared by placing a holey C film on a Cu TEM grid close to a burning MgO wick. Selected area electron diffraction patterns were recorded on a charge-coupled device (CCD) camera using a JEOL 2100 LaB_6 TEM. Fig. 3a shows bright-field TEM images of three crystals with cubic shapes viewed along [110], [100] and [111] directions for crystal sizes of approximately 160, 750 and 200 nm, respectively. In diffraction mode, the strongest diffracted beams were identified: (220) for the [111] orientation and (200) for the other two orientations. The chosen crystals have sizes well above the extinction distances for MgO of $\xi_{220} = 64.988$ nm ($V_{g,\,220} = 6.68$ V) and $\xi_{200} = 43.64$ nm ($V_{g,\,200} = 9.96$ V).

In order to obtain the results shown in Fig. 3b, a three-dimensional model of a cube with a lateral size of 80 nm was built in a volume of 128 × 128 × 128 pixels using a voxel size of 1 nm, with the normals parallel to the *x*, *y* and *z* axes. The use of a small simulation volume is computationally effective but the 3D model in Fig. 3 is smaller than the size of the experimental cubes shown in Fig. 3. Nonetheless, smaller models have a large shape factor in reciprocal space, thus increasing the resolution (the number of slices available) in the range of low values of s_g (or $s_{g,eff}$). Note that according to Eqs. (13) or (14) the contrast features

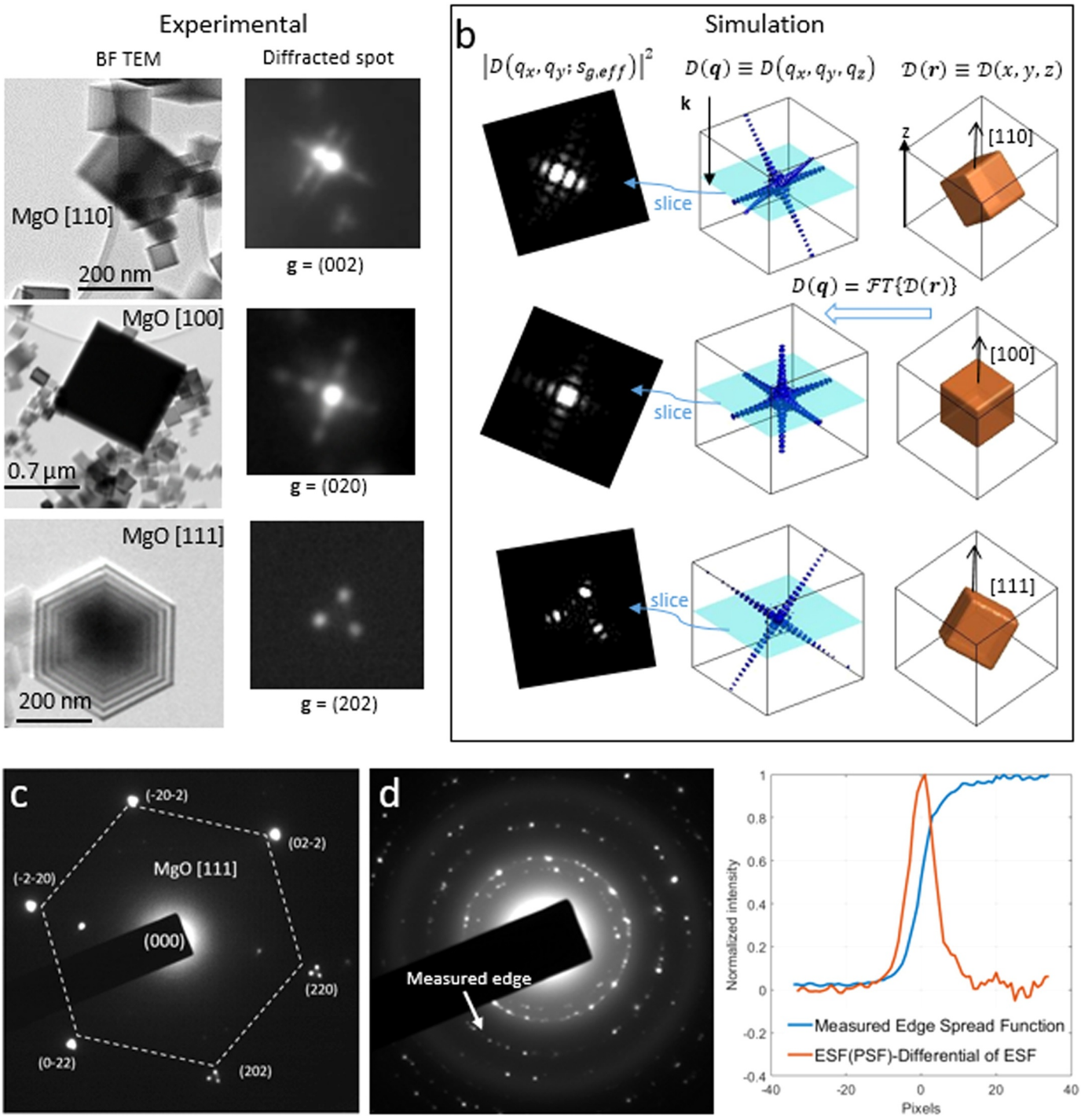

Fig. 3. (a) Experimental bright-field TEM images acquired at 200 keV of three MgO smoke crystals at different orientations. Right, the corresponding experimental diffracted spots acquired with a selected area diffraction aperture and a CCD camera. (b) Simulated diffracted spots calculated by slicing the shape factor of the 3D model of a cube oriented approximately along the same zone axes of the particles shown in (a), i.e., [110], [100] and [111]. The simulated fine structure of the spots display some differences with the experiment. (c) Full diffraction pattern of the MgO crystal oriented close to a [111] zone axis. The crystal is not diffracting in two-beam conditions, and the six reflections are excited at different deviation parameters (see discussion in the text). (d) Diffraction pattern of the powder of MgO crystals supported on amorphous carbon. The amorphous rings linked to the Contrast Transfer Function (CTF) of the objective lens are visible. Also, the background intensity is non zero, primarily because of a combination of the effect of the Thermal Diffuse Scattering (TDS) of the sample and the Point Spread Function (PSF) of the scintillator-camera system. The edge of the blocking pin was used to calculate the directional Point Spread Function shown in the right.

do not depend on the size of the crystal in real space but only on the deviation parameter selected to slice the shape factor. The incident electron beam in Fig. 3b is the z direction. The 3D model of the cube was rotated by 43° about the y direction to perform simulations close to [110], while a [111] orientation was obtained by rotating the 3D model by 45° about the y and x directions. Eq. (13) was applied to the 3D Fourier transforms (the shape factor $D(\boldsymbol{q})$) of the models. $D(\boldsymbol{q})$ for each orientation was computed in a volume of size 128 × 128 × 128 pixels using a reciprocal space pixel size of 0.0078 nm^{-1}. This value determines the minimum slice thickness $\Delta s_{g,\ eff}$ that can be used. Images

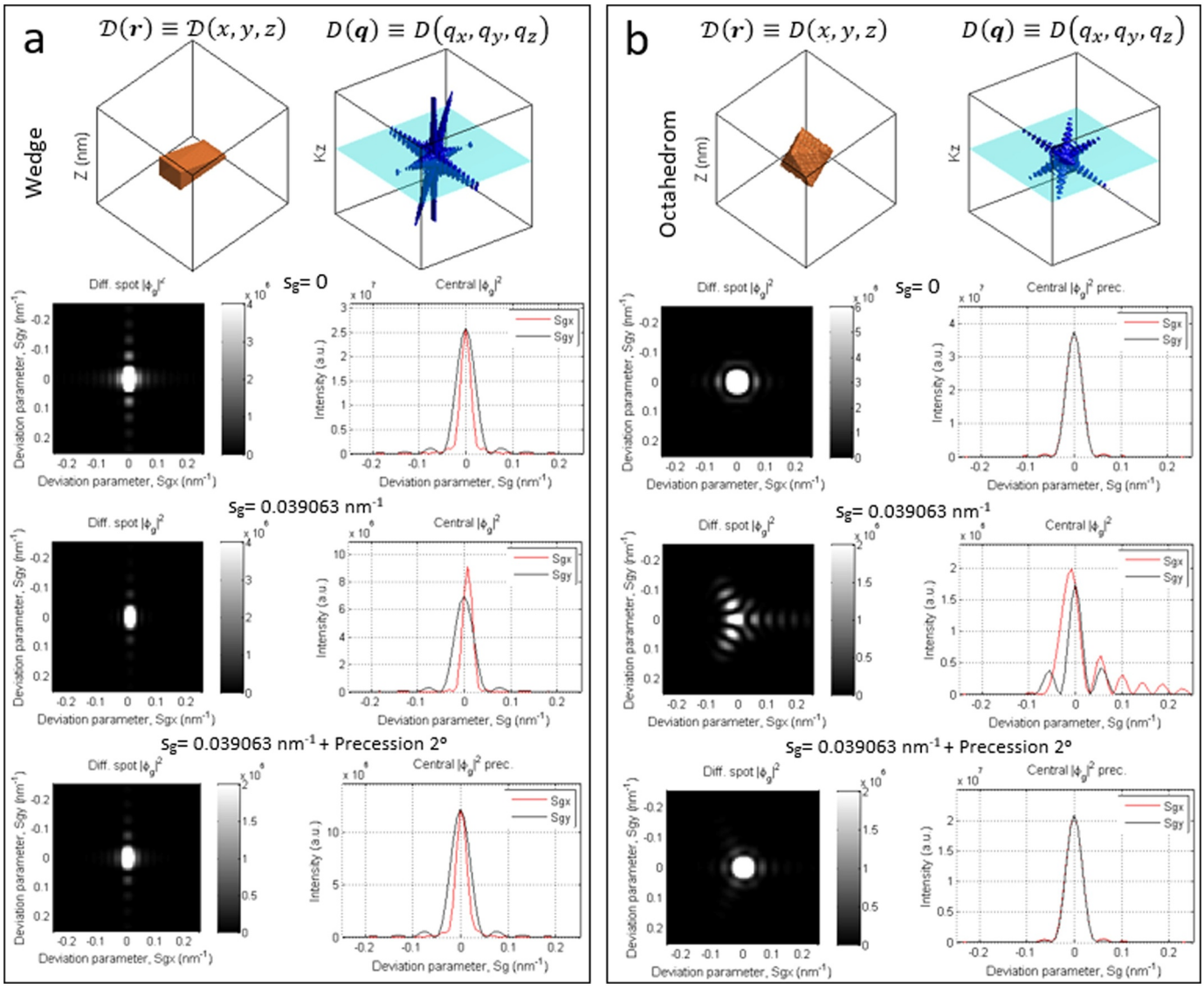

Fig. 4. (a) Simulations of the fine structure of a diffracted spot for a wedge-shaped crystal for deviation parameters of $s_g = 0$ and $s_g = 0.039063\ \mathrm{nm}^{-1}$. The right column shows intensity profiles along (s_{gx}, 0) and (0, s_{gy}). The lowest row shows a simulation about $s_g = 0.039063\ \mathrm{nm}^{-1}$ with a beam precession angle of 2°. (b) As for (a), but for an octahedral crystal with one of its faces oriented perpendicular to the incident electron beam direction. The shifts occurs whenever the crystal has asymmetrical shape.

and diffraction patterns were recorded at an accelerating voltage of 200 kV, corresponding to a de Broglie wavelength of electrons of $\lambda = 0.0025$ nm and a radius of the Ewald sphere $1/\lambda$ of $1/0.0025\ \mathrm{nm}^{-1}$, which is much larger than $|\boldsymbol{g}_{20\text{-}2}| = 6.718\ \mathrm{nm}^{-1}$ and $|\boldsymbol{g}_{002}| = 4.751\ \mathrm{nm}^{-1}$ for MgO. The Ewald sphere in the vicinity of the reciprocal lattice points can therefore be approximated with a plane. The slices of the diffracted spots in Fig. 3b were chosen by selecting slices of $D(\boldsymbol{q})$ perpendicular to the direction q_z, which best matched visually the symmetries of the fine structures of the experimental images. In order to reduce the high dynamic range of the intensities, approximately 10^7, the contrast and intensity of the images were adjusted.

The symmetries and features of the experimental images shown in Fig. 3a are well reproduced by the simulations although they display some differences. Fig. 3c shows a full diffraction pattern of the MgO crystal oriented close to a [111] zone axis. Four of the reflections are single big spots with a very large intensity, and the other two have a fine structure with three small spots at the corners of a triangle. The crystal is not diffracting in two-beam conditions, and the six reflections are excited with different deviation parameters. The four spots with large intensities must be cuts through the shape factor with a deviation parameter closer to zero. They look like single spots but in reality, each of them must have three spots very close to each other, and the saturation of the camera does hide their fine structure. But the experiment indicates also that the two-beam approximation, at least in qualitative terms, is a valid approximation for simulating the fine structure of the diffracted spots even though the crystal is not diffracting in two-beam condition.

The patterns of the experiment show also a lower level of contrast and detail compared with the simulated patterns. For example, the brightest spots at the central part of the simulations have squared shapes, while in the experiments the edges of the central parts are smoothed and look round. The origin of this difference may be because neither the background intensity due to thermal diffuse scattering (TDS) [19] nor the modulation transfer function (MTF) of the CCD camera were taken into account when performing the simulations [23]. Fig. 3d shows the diffraction pattern of the powder of MgO crystals supported on amorphous carbon. The latter is responsible for the observation of rings of intensity linked to the Contrast Transfer Function (CTF) of the objective lens that modify the background intensity of the

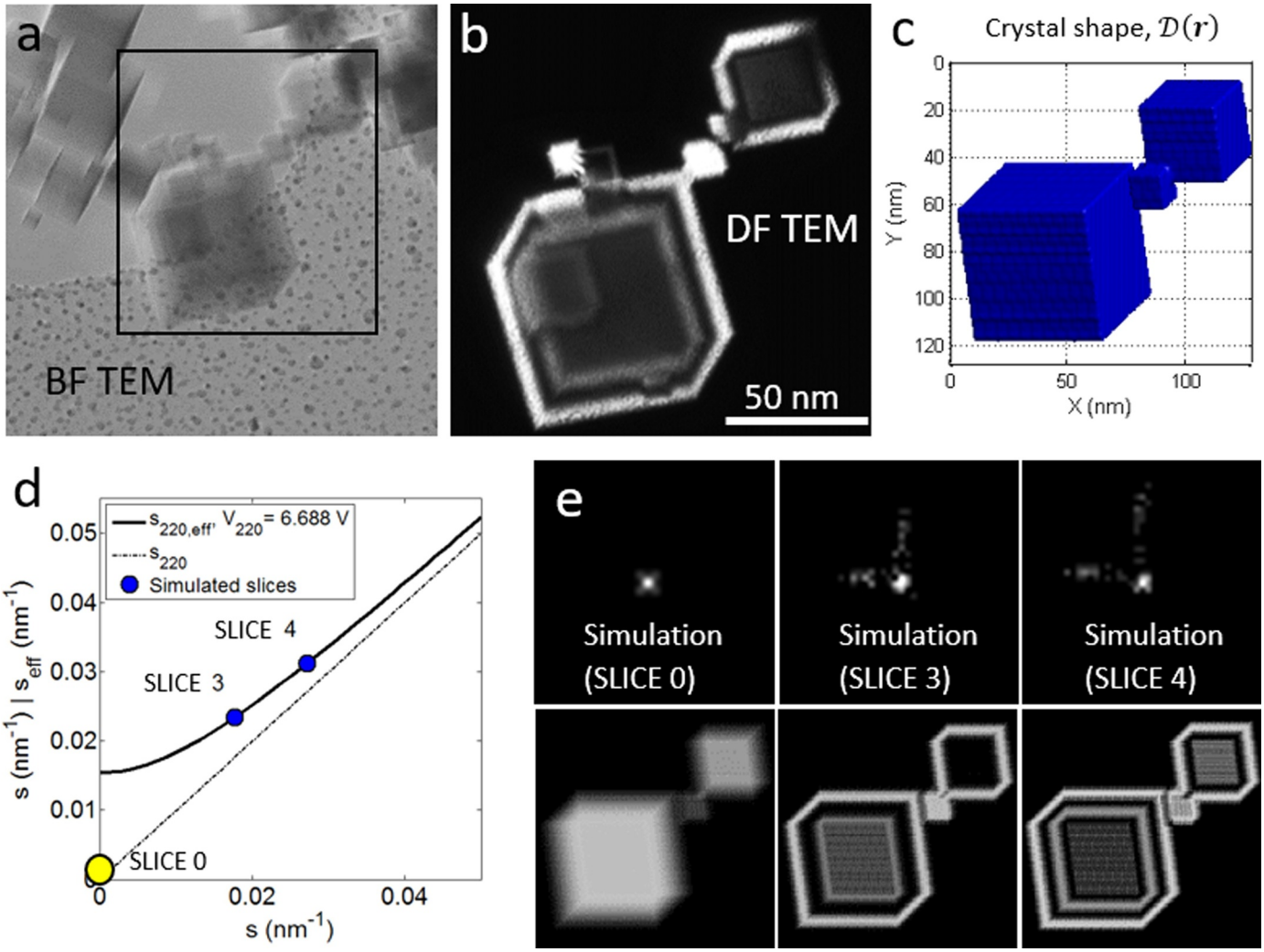

Fig. 5. (a) BF TEM image of a sample of MgO cubes. (b) DF TEM image of the inset in (a) obtained by inserting an aperture at the diffraction plane and selecting one (220) diffracted spot. The cubes are oriented close to a [1 3 3] zone axis. (c) 3D model of shape of three cubes built and spatially oriented to resemble the BF image shown in (a). (d) The deviation parameter s_g and the effective deviation parameter $s_{g,\,eff}$ plotted for the kinematical and dynamical cases using Eq. (11) for $\boldsymbol{g}$ = (2 2 0), V_g = 6.688 V and ξ_g = 64.988nm. (e) The simulation of three diffracted spots and the corresponding DF images was calculated by inverse Fourier transforming slices (called slices 0, 3 and 4 in (d)) of the shape transform of the 3D model. Slice 0 only exists in the kinematical approximation (yellow circle on the dotted curve in (d)) and corresponds with uniform contrast (without *Pendellossung* fringes). Experimentally, we observed that the largest crystal displayed *Pendelossung* fringes at any value of s_g what confirms that dynamical diffraction dominates for that crystal. Nevertheless, smaller cubes displayed uniform intensity at certain orientation, what indicates that kinematical approximation is valid for those sizes of the crystals.

diffracted spots. Also, TDS of the carbon film and of the crystals, being one of the sources of normal absorption contribute to the intensity observed in the background of the pattern. TDS is one of the main sources of normal absorption and as it is shown theoretically in Eqs. (25) and (31), normal absorption is a non constant function of reciprocal coordinates that attenuates the diffracted intensities. Moreover, the amount of image detail of the pattern that is transferred to the recorded image is strongly dependent of the optical properties of the detector system. The MTF of one detector is the Fourier Transform of its Point Spread Function (PSF). In non ideal (real) detectors the Point Spread Function (PSF) is responsible for a loss of detail of the image. In TEM it may be originated for instance by the multiple scattering of an electron impinging on the scintillator of the CCD camera. In Fig. 3d is shown an estimation of the PSF in one direction using the slanted-edge method. The Edge Spread Function (ESF) was measured as the intensity profile of one edge of the blocking pin (white arrow in Fig. 3d), and the directional PSF was calculated as the derivative of the ESF profile. The FWHM of the peak of about 8 pixels gives a estimation of the smoothing effect of the PSF on the recorded diffraction pattern. In order to evaluate more accurately the influence of the PSF and the TDS on the simulated images, future experiments could be carried out performing simulations using Eq. (25), cooling the sample to reduce TDS and with direct detectors which have better MTF (narrow PSF) [24].

3.1.2. Simulations of the distorted fine structures of diffracted spots with and without precession

The fine structure of diffraction spots (splitting, symmetries and shifts) have been explained using the concept of dispersion surfaces. The method of slicing the shape factor introduced in this work can be used also to understand the factors that influence the positions and shapes of diffracted spots that are frequently observed experimentally [12,25]. This information is important for accurate metrology from diffraction patterns (using both X-rays and electrons). Diffraction patterns are used for the identification of crystal phases that depends on the accurate measurement of reciprocal distances (moduli $|g|$) and angles of $\boldsymbol{g}$ -vectors between the direct beam and diffracted beams. Also, small shifts of $|g|$ can be used for measuring crystal distorsions that can be linked for example to small compositional changes [26].

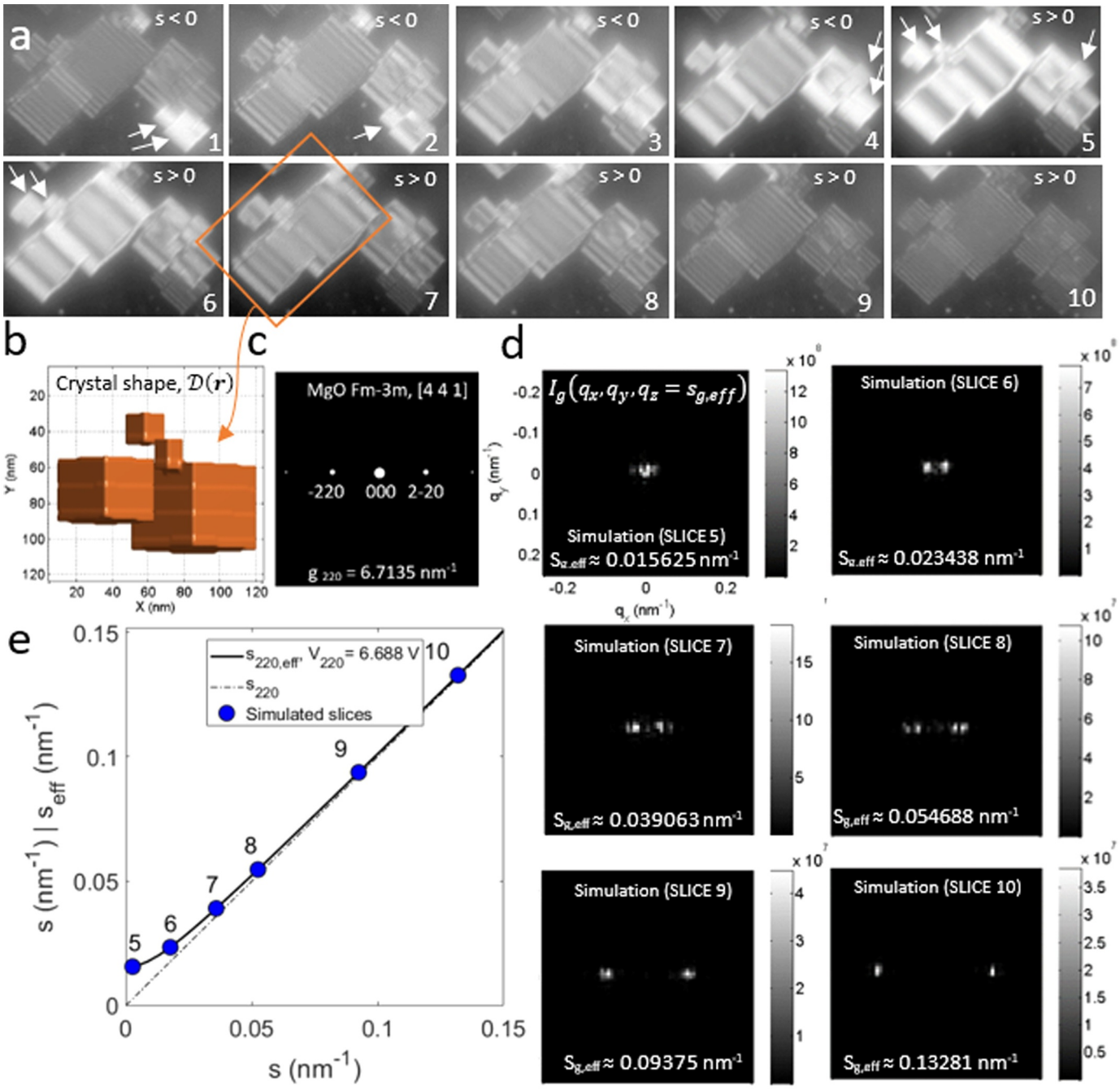

Fig. 6. (a) Tilt series of experimental DF TEM images of MgO cubes acquired with a tilt step of 0.05° ($\Delta s_{220} = g_{220}\,\Delta\theta = 0.0059\,\mathrm{nm}^{-1}$). (b) 3D model of shape of four cubes built and spatially oriented to resemble the area of the DF image shown inside the rectangular box in the image number 7 in (a). (c) Simulated diffraction pattern of MgO cube oriented close to a [4 4 1] zone axis. The unit cell has Fm-3 m symmetry and the simulated diffraction pattern show that the strongest reflections are the (220)-type. This reflection has an extinction distance at 200 keV of 64.988 nm. (d) Six simulated images of the fine structure changes of a (220) spot as a function of the deviation parameter. They were calculated by taking the modulus square of slices of the shape transform of the 3D model at the values of the deviation parameter s indicated on the curve shown in (e). These results can be replicated using the *Matlab* code provided in the Appendix.

Fig. 4a and b show simulations of diffracted spots for a wedge-shaped crystal and a crystal with an octahedral shape, respectively, for three different experimental conditions. The first row shows three-dimensional models and corresponding shape factors. The next two rows show simulations for deviation parameters of $s_g = 0$ (i.e., for the kinematical case) and $s_g = 0.39063\ \mathrm{nm}^{-1}$. Intensity profiles were generated from each of the simulated diffractograms along the (s_{gx}, 0) and (0, s_{gy}) directions. The fourth row in Fig. 4 shows a simulation of the effect of precessing the electron beam by a tilt of 2° for a crystal with $s_g = 0.39063\ \mathrm{nm}^{-1}$ using Eq. (15). Fig. 4 reveals the presence of shifts, high intensity subsidiary peaks and peak broadening when the deviation parameter is non-zero, even for perfect crystals with uniform composition. The shifts of the peak maxima and asymmetries of the fine structure happen whenever the crystal shape seen along the electron beam direction is asymmetric. The effect is more visible for large values of s_g. For example, the shape transform of the wedge is elongated in a direction perpendicular to the wedged facet. As the deviation parameter increases from zero, the corresponding slice will show a peak of intensity that shifts. Finally, we note that for increasing the accuracy of the simulations of large crystals the Eq. (15) should be used together

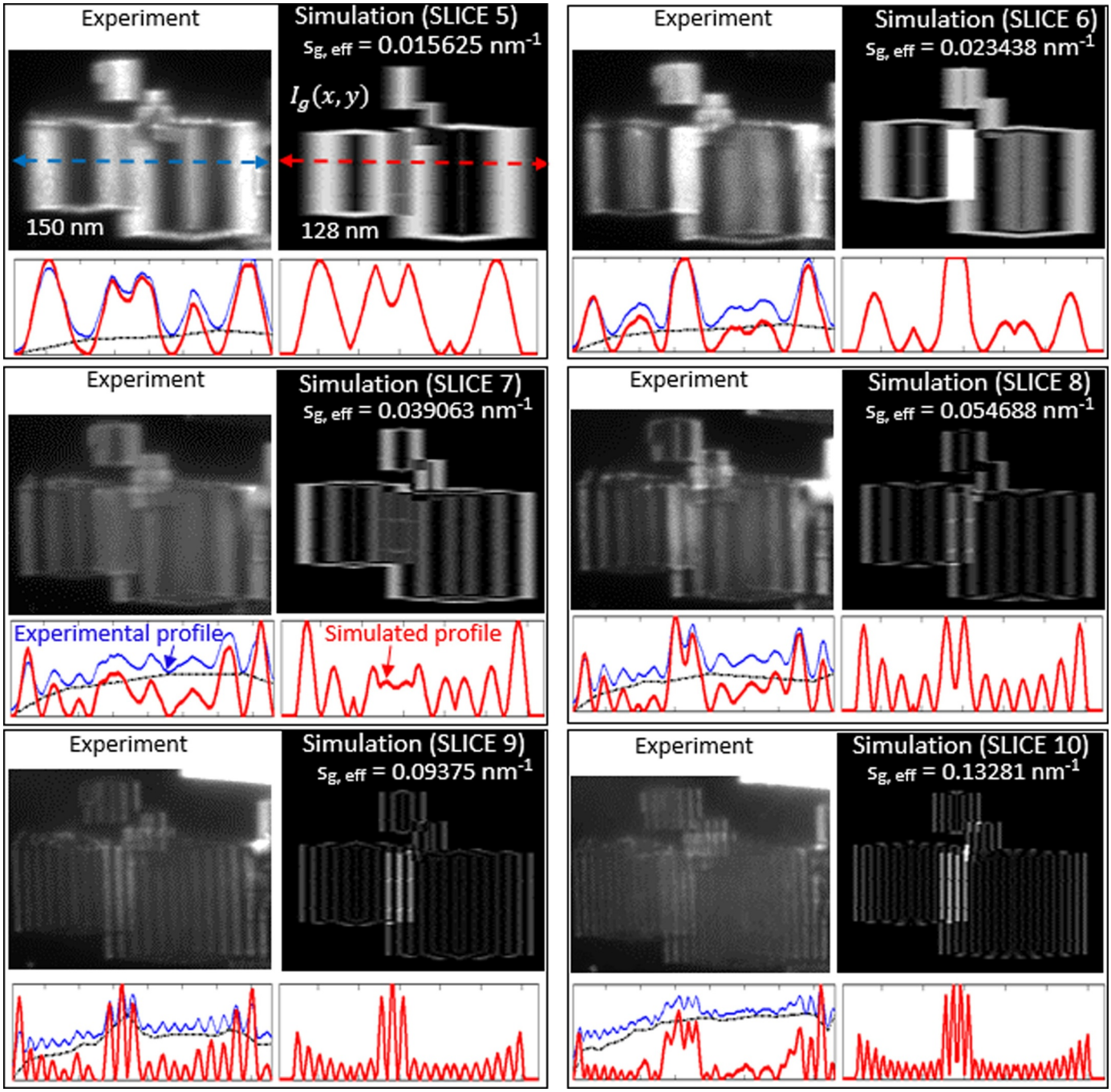

Fig. 7. Experimental and simulated DF TEM images at six different values of the deviation parameter of the MgO cubes shown in Fig. 6. The simulation of the DF images was calculated by inverse Fourier transforming slices of the shape transform of the 3D model with a normal absorption coefficient $\xi_o' \approx 4\ \xi_g$, and normalized to 1. The slices were chosen to best fit the contrast features observed in the experimental images in terms of the number, shape and intensity of the *Pendellossung* fringes. Below each image, are plotted the intensity profiles (in red colour) measured on a central line perpendicular to the fringes as indicated with the dashed line in the top left images. The splitting of (and the separation between) the diffracted spot shown in Fig. 6 is a measure of the spacing between *Pendellosung* fringes. These results can be replicated using the *Matlab* code provided in the Appendix.

with Eq. (24) in which normal absorption has been included.

3.2. Simulations of dark-field images

3.2.1. Pendellosung fringes of an ensemble of MgO crystals

The image in Fig. 5a is an experimental bright-field (BF) TEM image of smoke of MgO crystals deposited on a thin carbon film. The dark-field (DF) TEM image in Fig. 5b was formed selecting a (220) strong reflection with the objective aperture. The cubes are similarly oriented in a [113] zone axis geometry according with the FCC cubic structure of MgO (Fm-3m, a = 4.213 Å).

The simulations shown in Fig. 5 where obtained as follows. A 3D model ($\mathcal{D}(\boldsymbol{r})$) of three cubic shapes was built with a volume of 128 × 128 × 128 pixels and a pixel size of 1 nm (see Fig. 5c). The cubes were resized and rotated to match the orientation of the crystals located inside the square shown in Fig. 5a. The three-dimensional Fourier transform (shape transform, $D(\boldsymbol{q})$) of the 3D model was computed resulting in a volume with a size of 128 × 128 × 128 pixels and a

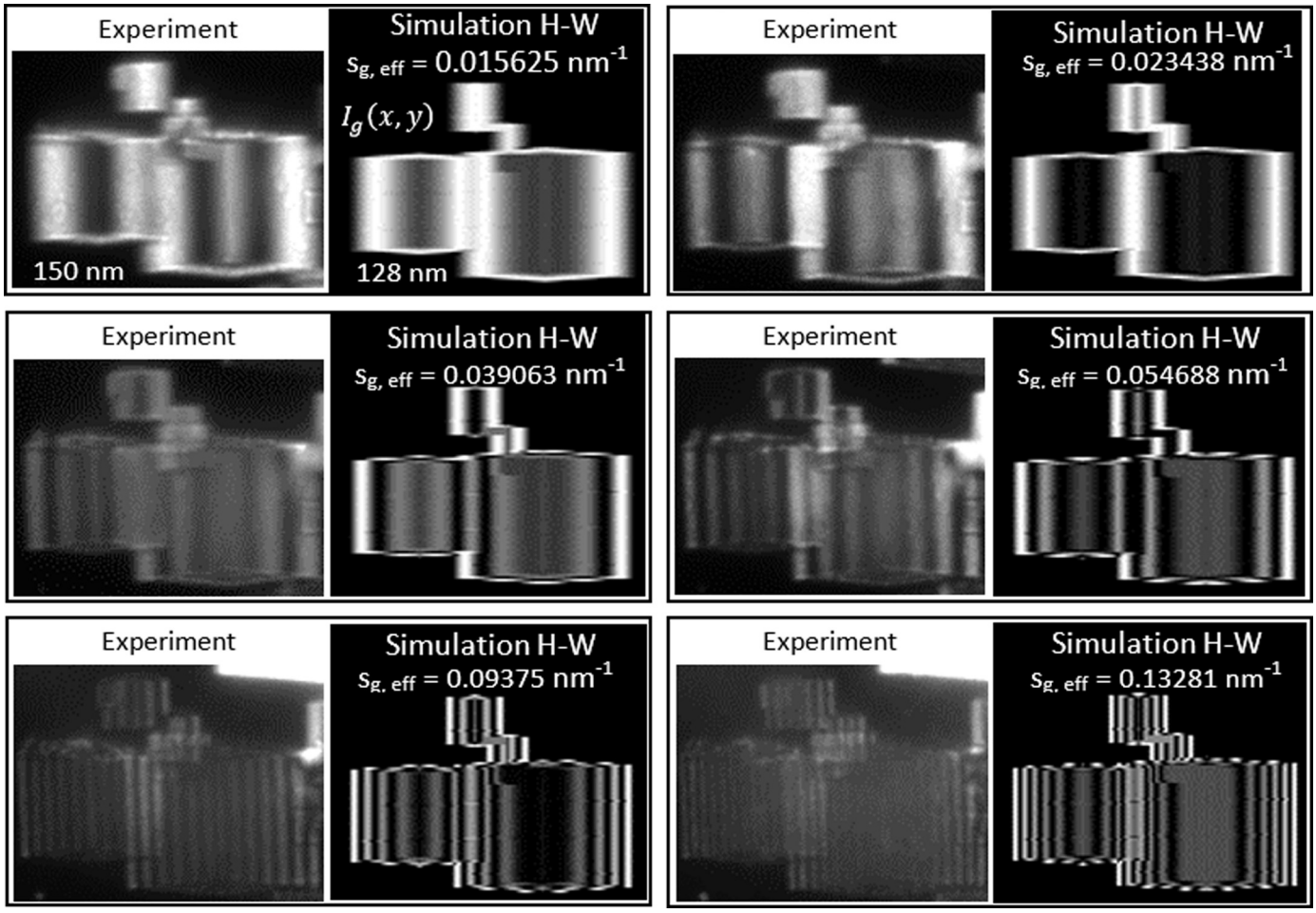

Fig. 8. Experimental and simulated DF TEM images at six different values of the deviation parameter of the MgO cubes shown in Fig. 6. The simulation of the DF images was calculated using Howie-Whelan Eq. (22) and with a normal absorption coefficient $\xi_o' \approx 5\,\xi_g$. The slices were chosen to best fit the contrast features observed in the experimental images in terms of the number, shape and intensity of the *Pendellossung* fringes. The match between experiment and simulation fails when the value of the deviation parameter is larger than approximately 0.0234 nm^{-1}.

reciprocal pixel size of 0.0078 nm^{-1}. This value determines the minimum thickness Δq of the slicing scheme for the pixel resolution used. The DF TEM images were simulated using Eq. (20) by selecting the slices of $D(\boldsymbol{q})$ perpendicular to the direction q_z that best matched the experimental images, and normalized to 1. While experimentally it has been shown that typically $\xi_o' \approx 10\,\xi_g$ [20], a better match in our experiments between the experimental and simulated images was found using lower values $\xi_o' < 10\,\xi_g$. The images of the diffracted spots displayed in Fig. 5e were calculated without absorption using Eq. (14) at the same values of $s_{220,eff}$ found optimal to simulate the DF TEM images.

3.2.2. Simulations of a tilt series of dark-field TEM images using the single slice approach

The collection of images numbered 1–10 in Fig. 6a is an experimental tilt series of DF TEM images of similarly oriented MgO crystals. The objective aperture was used to select a (220) strong reflection that agrees with the geometry of the cubes and the fcc cubic structure of MgO (Fm-3 m, a = 4.213 Å) oriented in a [4 4 1] zone axis (see Fig. 6c). The tilt series was acquired at increasing tilt angles of the sample holder using a tilt step of 0.05°, effectively varying the deviation parameter s_{220} in steps of $\Delta s_{220} \approx 0.0059\,\text{nm}^{-1}$. A detailed two-beam simulation of the series of images (and the fine structure of the diffracted spot) was carried out (Fig. 7). The simulations can be replicated using the *Matlab* code provided in the Appendix.

The results shown in Figs. 6d and 7 were obtained as follows. A 3D model of four cubic shapes was built with a volume of 128 × 128 × 128 pixels and a pixel size of 1 nm (see Fig. 6b). The cubes were resized and rotated to match the size and orientation of the crystals located inside the square of the image 7 in Fig. 6a. The three-dimensional Fourier transform (shape transform, $D(\boldsymbol{q})$) of the 3D model was computed resulting in a volume with a size of 128 × 128 × 128 pixels and a reciprocal pixel size of 0.0078 nm^{-1}. This value determines the slice thickness Δq of a single slice. And the intensity of the DF TEM images normalized to 1 in Fig. 7 were simulated using Eq. (20) by selecting the slices of $D(\boldsymbol{q})$ perpendicular to the direction q_z that best matched the experimental images. For the simulation of the DF TEM images we adjusted the value of absorption until a best much was found between the contrast of the line profiles measured on the simulated and experimental images using a value $\xi_o' = 5\,\xi_g$. The experimental (blue colour) and simulated (red colour) profiles are shown below each image. Experimental images have a background intensity due to the carbon layer used to support the crystals. For comparing the experimental with the simulated profiles, the background profile of each image (black lines) was constructed by interpolating the throughs of the curves. The red profiles below each experimental image were obtained by subtracting the corresponding background line. The images of the diffracted spots displayed in Fig. 6d were calculated using Eq. (14) at the same values of $s_{220,\,eff}$ found optimal to simulate the DF TEM images.

The number and structure of *Pendellosung* fringes in Fig. 7 changes with tilt what indicates that the shape factors of each crystal have been sampled. The tabulated value of the extinction distance of $\boldsymbol{g}$ = (220) of

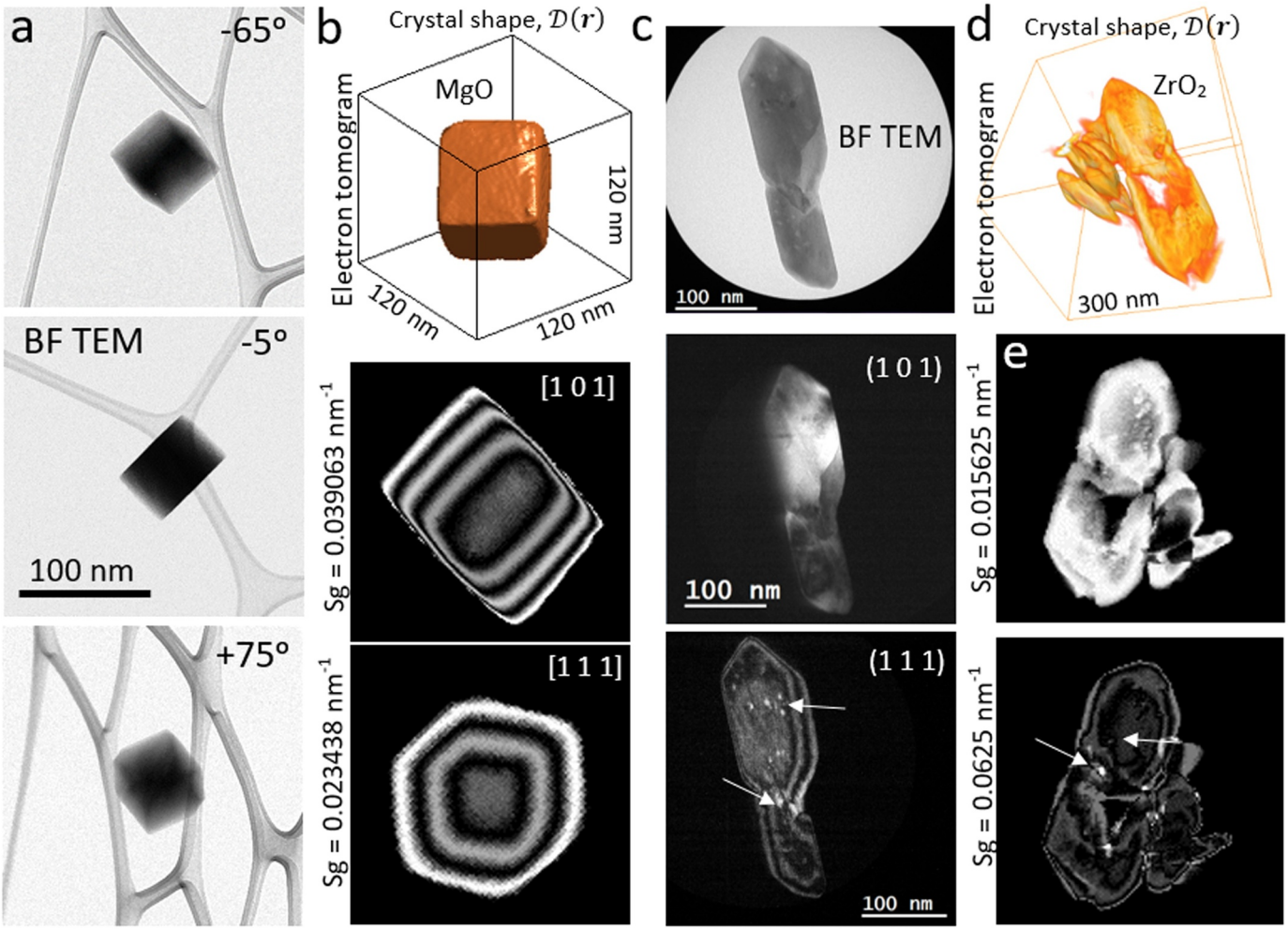

Fig. 9. (a). The shape function $\mathcal{D}(\boldsymbol{r})$, required for performing a simulation within the single slice framework described in this work can be obtained experimentally using electron tomography. (a) Three images of an MgO cube representative of a tilt series of BF TEM images acquired between −65 to 75°. (b) Isosurface visualization of the 3D model of the electron tomogram of the cube. Below, two DF TEM images of the cube obtained for two different orientations of the 3D model and using the single slice approach. (c) Experimental BF TEM image of one crystal of ZrO_2. Below, two DF TEM images acquired selecting with the objective aperture a (1 0 1) or a (1 1 1) reflection. (d) Voltex visualization of an ensemble of ZrO_2 crystals measured with HAADF STEM tomography. (e) DF TEM images simulated using the single slice approach for two values of the deviation parameter.

MgO, ξ_{220}(MgO) = 64.98 nm, was used to plot the s_{220} - $s_{220,\ eff}$ curve of Fig. 6e. Each simulated image have a different value of s_{220} or of $s_{220,\ eff}$ depending on whether a crystal is diffracting under kinematical or dynamical conditions, corresponding with points on one of the two curves of Fig. 6e. The two largest crystals in Fig. 7 display *Pendellosung* fringes whose number decreases from slice 1–5, and when the deviation parameter changes sign the number of fringes increases again from slice 6–10 (see Fig. 6a). In none of the experimental images the two large crystals display uniform contrast that would happen only if $s_g = 0$, and indicates that those crystals are scattering dynamically (the effective deviation parameter is $s_{220,\ eff} \neq 0$). This observation agrees with the fact that those crystals have thicknesses that are larger than ≈ 65 nm (the extinction distance ξ_{220} of MgO). On the contrary, *Pendellosung* contrast of smaller crystals (marked with white arrows in Fig. 6a) disappears at certain tilt angles and display uniform bright contrast. This is an indication that the smaller crystals are diffracting under kinematical conditions what agrees with the fact that those crystals have thicknesses that are below ≈ 65 nm (the extinction distance ξ_{220} of MgO). Notice that in the Figs. 6–8, the models of the crystals are made of several crystals while a single slice is calculated. The 'single slice approach' does not require choosing in advance if the scattering is kinematical or dynamical. The shape factor does not change, the free parameter is the slice chosen to cut through reciprocal space. What changes is which slice is being excited for a given orientation/tilt of the crystal. The shape factor of the crystals $D(\boldsymbol{q})$ in Figs. 6–8 is a convolution of four shape factors with exactly the same shape but with different sizes, one for each of the crystals. Smaller crystals have bigger shape factors and viceversa. When a slice is taken in Fourier space, the four shape factors are sliced differently giving rise to different contrast features.

The experimental tilt series combined with the simulations of Fig. 6 can be used to estimate the extinction distance of a reflection. For example, the contrast of the *Pendellosung* fringes of the largest crystal in Fig. 6a is dynamical and it has an inflection point at the tilt shown in image 5. Thus, the deviation parameter value of image 5 obtained with simulations must then be close to the minimum of the curve $s_g - s_{g,eff}$ which is equal to $s_{g,eff}$(min)= $1/\xi_{220}$(MgO). Then ξ_{220} (MgO simulated) = $1/0.015625\ \text{nm}^{-1} \approx 64$ nm that is close to the tabulated value of 64.98 nm.

Finally, let's note that a better fitting between experiment and simulations can be obtained. The single slice method proposed is based on building a numerical model of the shape of a crystal (not analytically). The results presented were obtained using 3D models with a numerical resolution of 128 × 128 × 128 pixels. The 3D Fourier transform of the model will be also discretized with a resolution of 128 × 128 × 128 pixels. And the maximum number of slices in reciprocal space is 128. In order to obtain a better fitting, the number of

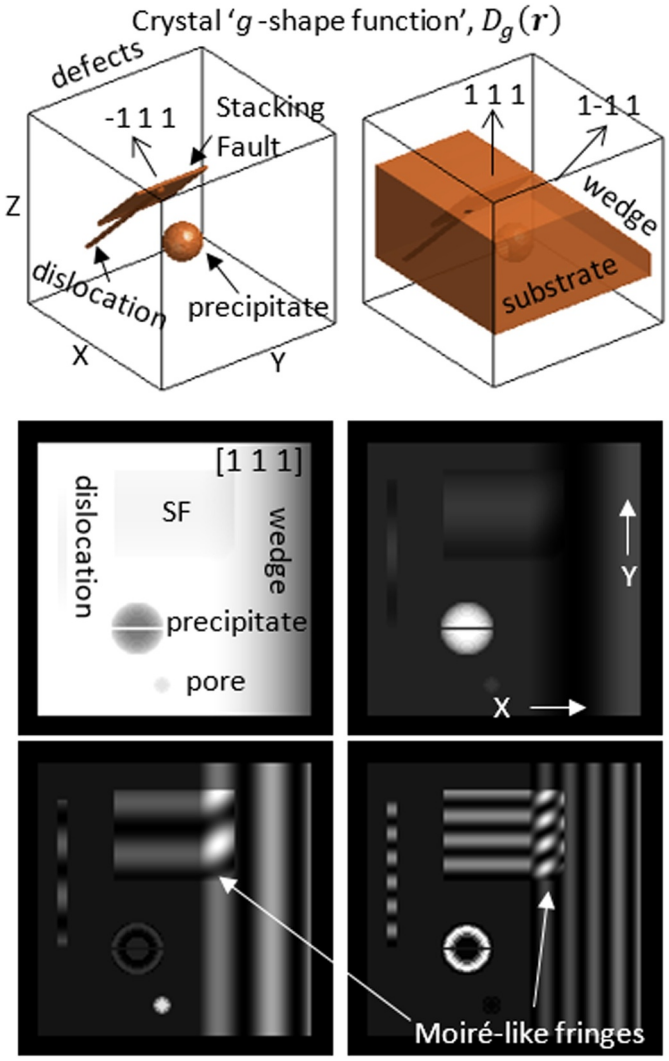

Fig. 10. Top row, model in 3D (amplitude) simulating the shape function of four types of defects for a family of ***g***-planes: a dislocation, a stacking fault (SF), a pore and a coherent precipitate. The defects are contained in a planar slab (substrate) that has a wedge shape in one side. Below, several DF TEM images simulated using the single slice approach described in the text. The 4 slices show the variation of the contrast features of the defects for increasing values of the deviation parameter (clockwise).

pixels of the 3D models must be increased, for example up to 256 × 256 × 256, effectively doubling the resolution (dividing by two the thickness of the slices).

3.2.3. Simulations of a tilt series of dark-field TEM images using Howie-Whelan equation

Next we performed the simulation of the collection of images numbered 1–10 in Fig. 6a using the 3D model of Fig. 6b and the two-beam form of the Howie-Whelan equation given by

$$I_g = |\phi_g|^2 = \frac{\pi^2}{\xi_g^2}\frac{sin^2\ \pi t s_{g,eff}}{(\pi s_{g,eff})^2}\cdot e^{\frac{-2\pi}{\xi'_o}z(x,y)}, \tag{33}$$

where it has been added the exponential term that accounts for normal absorption. The calculated images whose intensities are normalized to 1 are shown in Fig. 8. We found that the match between experiment and simulation diverge when the value of the deviation parameter is larger than approximately 0.0234 nm^{-1}. Specifically, the central part of the two larger MgO crystals do not display the structure (number, width and position) of the thin *Pendellosung* fringes observed in the experimental images. The result seems to corroborate that in some situations the Howie-Whelan equation can fail to reproduce image details under weak beam conditions even for perfect crystals [9,10,22].

3.2.4. Measuring the shape factor using electron tomography

We have shown that the Eqs. (14) and (17) (or (20) and (25)) can be used to simulate the images of a diffracted beam formed at the focal and image planes of a TEM. The critical step is that of obtaining an accurate model of the real shape of the crystal. This can be done creating numerically a 3D model as shown in Figs. 1–7. Alternatively, one can measure the 3D model experimentally using for example electron tomography. Fig. 9a shows three representative images of a tilt series of BF TEM images of an MgO cube. The series was pre-processed for minimising the background intensity [27], and Fig. 9b shows an isosurface visualisation of the cube obtained by segmenting the reconstructed tomogram. The two DF TEM images were calculated rotating the model close to a [1 0 1] and a [1 1 1] zone axis, and extracting one slice of the shape factor (Eq. (20)) at each orientation using the single slice approach.

Fig. 9c shows a BF TEM image of a ZrO_2 crystal (monoclinic), and two experimental DF TEM images acquired with two different values of the deviation parameter (e.g., by selecting different diffracted spots with the objective aperture). Fig. 9d shows the 3D model of an ensemble of crystals of the same sample measured using HAADF STEM tomography and that was used for calculating (Eq. (20)) the DF TEM images of Fig. 9e. The tomogram was Fourier transformed and the 3D shape factor was sliced at two values of s_g. The crystals have elongated shapes with a high width/thickness ratio, contain pores and surface irregularities (thickness changes and pits). All these morphological features are visible in the DF images as points with high brightness (marked with arrows), *Pendellosung* fringes with non-uniform spacing, and speckle contrast. And the same features are reproduced in the simulated images.

3.2.5. Simulation of defects in crystals: slicing the "g-shape factor"

Fig. 10a shows an example of the application of Eq. (32) for simulating dark-field contrast in two-beam conditions of four types of defects. The top row shows the amplitude of the complex shape function $\mathcal{D}_g(\boldsymbol{r})$ (see definition 28) of a reflection ***g*** of a crystal.

The substrate is modelled as rectangular region with a value of 1 that can represent a reflection ***g*** = (1 1 1) of a crystalline substrate with face-centred cubic structure in a [111] zone axis. One side of the substrate has a wedge with orientation (1 −1 1) (45°' inclination). Inside the substrate the core of a linear dislocation is modelled by setting to zero a line inside the substrate. A planar stacking fault (SF) defined by a plane with normal (−1 1 1) is modelled by setting to zero a planar area inside the substrate. A pore has been modelled by setting to zero a small spherical region inside the substrate.

The coherent precipitate with spherical shape is defined by those points $(x,\ y,\ z)$ of the substrate that are at a distance $d = \sqrt{(x-x_o)^2 + (y-y_o)^2 + (z-z_o)^2} < R_o$ from a point $(x_o,\ y_o,\ z_o)$. Strain contrast originated by the precipitate is due to the displacement of the family of ***g***-planes. Theoretical models show that the displacement field inside a coherent precipitate is radial and increases linearly with d, i.e., $R = \varepsilon\ d$ for $d \le R_o$ being ε a value that describes an isotropic strain [1]. The phase change (Eq. (28)) of the wave scattered at a point $(x,\ y,\ z)$ inside the precipitate is given by $\boldsymbol{g}\cdot\boldsymbol{R}(\boldsymbol{r}) = g\,R(\boldsymbol{r})cos\varphi = g\,\varepsilon\,d\,cos\varphi$. Let's consider that we forming a DF TEM image using a reflection ***g*** that is parallel to the y-axis. In spherical coordinates, the angle φ and the y-coordinate of a point P located at a distance d from the origin are related simply as $y = d\ cos\varphi$, and the phase factor is given by $\boldsymbol{g}\cdot\boldsymbol{R}(\boldsymbol{r}) = g\,\varepsilon|y - y_o|$, which is the function used for the simulation of the precipitate shown in Fig. 10 with ε = 0.05.

Although the 3D model used for the simulations in Fig. 10 is very simple, the contrast of the calculated images display several contrast features typically observed for these types of defects. The ondulatory

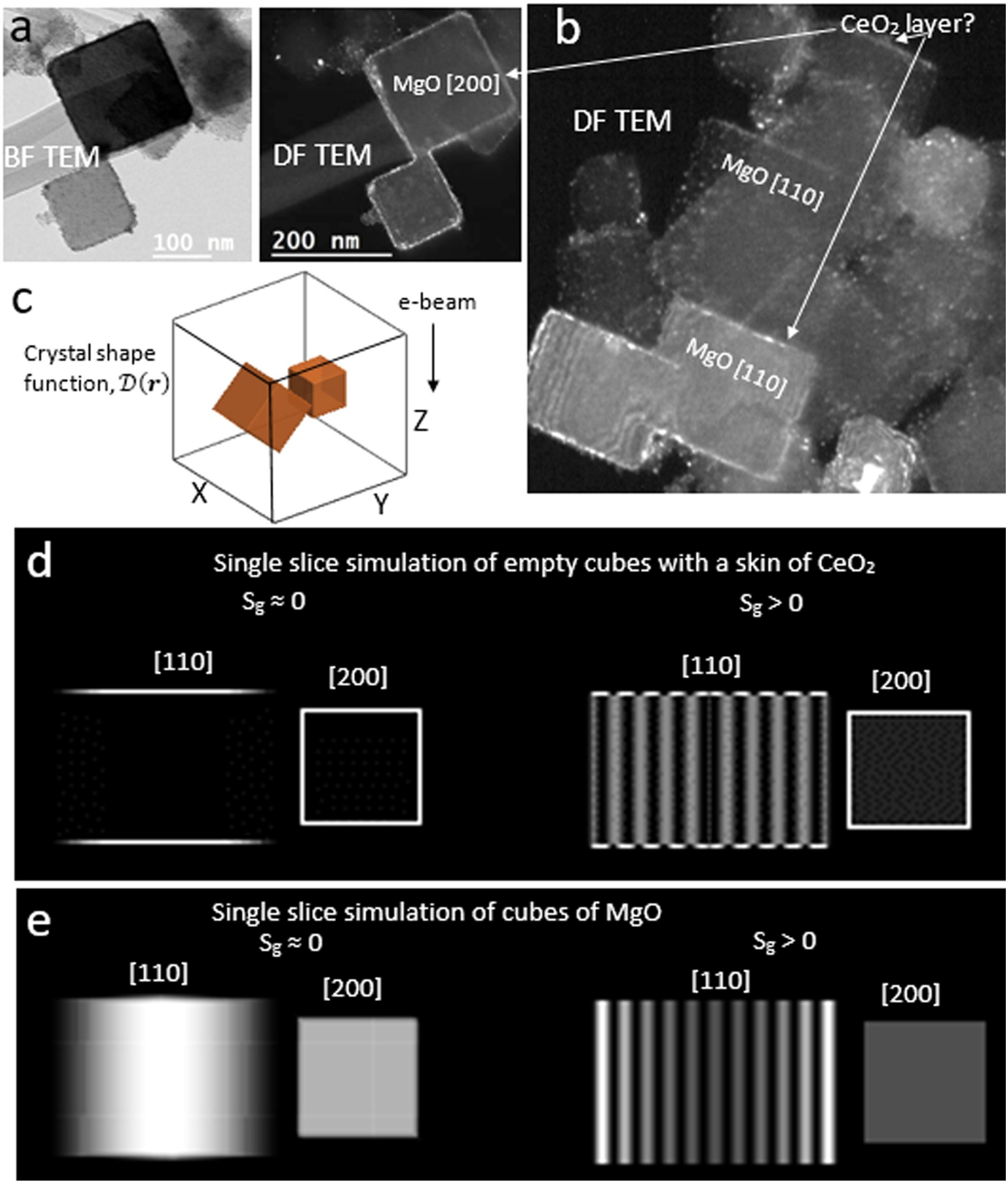

Fig. 11. (a) Top, BF and DF TEM images of two MgO crystals on [200] orientation with sizes of about 120 and 200 nm. The crystals have a thin skin of CeO_2. (b) DF TEM images of an ensemble of MgO/CeO_2 crystals. Several of them are oriented close to a [110] zone axis. A bright rim surrounds most of the crystals. (c) 3D model of the shape function $\mathcal{D}(\boldsymbol{r})$ of two cubes in [100] and [110] orientation (the Z-axis is the beam direction). (d) Calculation of DF TEM images using the 3D model shown in (a) in which only a thin skin was set to 1 ($\mathcal{D}(\boldsymbol{r} \in surface) = 1$) and the inside was set to 0 ($\mathcal{D}(\boldsymbol{r} \notin surface) = 0$). The simulations display the bright rim and *Pendellosung* fringes observed in the experimental images. (e) Calculation of DF TEM images using the 3D model shown in (a) in which the cubes are solid, $\mathcal{D}(\boldsymbol{r} \in cube) = 1$). The simulations do not display the bright rims observed in the experimental images. All the simulated images are normalized in intensity to 1.

contrast of the dislocation increases with the deviation parameter. The contrast of the coherent precipitate has a central band and two side-bands. The pore can be dark or bright as in Fig. 9. And the stacking fault shows *Pendellosung* fringes which interfere (Moiré-like) with the fringes of the wedge at the area of intersection of both defects.

3.2.6. Simulation of DF TEM contrast of crystalline monolayers of CeO_2

Finally, we have applied the single slice approach to investigate the contrast of DF TEM images of a sample of MgO cubes synthetized with an atomically-thin crystalline layer of CeO_2 which recovers their external surface [28]. The sample was prepared as a powder and deposited on a Cu grid with lacey carbon. Fig. 11a and b show representative BF and DF TEM images of the sample. The DF TEM images were acquired selecting with the objective aperture a diffracted spot corresponding to the crystalline phase CeO_2. Most of the cubes are in [110] and [200] orientations, and their perimeters are surrounded with rims of bright intensity. The two cubes in the left of Fig. 11b show also *Pendellossung* fringes. Using energy-dispersive x-ray spectroscopy in STEM mode it was possible to measure a higher signal of Ceria at the surface of the cubes. We have used the single slice approach to answer the following questions –can we link the bright rims with the Ceria layers? Can we use DF TEM contrast as a method for detecting the presence of atomically-thin layers?

First, a 3D model of the CeO_2 layer was defined. Fig. 11c, shows a model of two MgO cubes with their shapes orientated like [200] and [110] zone axes, being Z-axis the direction of the electron beam. The thin shell around a cube was modelled by setting the shape function $\mathcal{D}(\boldsymbol{r})$ to 0 inside the cubes, and $\mathcal{D}(\boldsymbol{r})$ to 1 just for a surface layer of 1 nm. Fig. 11d shows the single slice simulation of the CeO_2 for two values of the deviation parameter. The simulation replicates the experiment correctly when $s_g \approx 0$, i.e., the continous bright rims appear surrounding the darker cubes. Moreover, the simulation whith $s_g > 0$ displays *Pendellossung* fringes and a discontinuous bright rim at the top and bottom surfaces of the cube. These features appear also in the experiment. All the features are visible simultaneously in the Fig. 11b and indicates that different cubes are diffracting under different conditions may be due to small differences in size or tilt. For comparison, Fig. 11e shows the single slice simulation of solid cubes of MgO for two values of the deviation parameter, and the simulations do not show the bright rims observed experimentally when $s_g \approx 0$, neither for $s_g > 0$.

Nevertheless, some experimental contrast features cannot be explained only with the model of a thin crystalline shell of Ceria. For instance, one of the cubes on the left side shows bright rims at the left and right side edges. Also, some of the cubes display the bright rim at only one of the surfaces. The growth of the thin layer of Ceria is expected to be coherent with the MgO support, and preferential orientation is likely, but synthesis is not perfect, the MgO surfaces are irregular and CeO_2 forms also a polycrystalline phase of small crystals. These nanocrystals scatter on the surfaces of the cubes and attach coherent and incoherently to the MgO. They produce the bright mottled contrast observed in Fig. 11 and when the cubes are seen edge-on they will seem to form a continuous layer of bright intensity, similar to the bright rims observed. Moreover, the cubes shown in Fig. 11a and b seem to have rounded edges. Those edges are like narrow facets and when the crystals are viewed close to a [110] zone axis orientation they can diffract and appear like bright rims.

4. Conclusions

We have presented a simple method that can be used to calculate dynamical complex amplitudes $\phi_g(q_x, q_y)$ and $\phi_g(x, y)$ diffracted by a crystal under two-beam conditions Eqs. (13) and ((16) respectively). Eqs. (14) and (17) (or (20) and (25) including normal absorption) provide the image intensities formed at the focal and image planes of a TEM. The method is non-atomistic and hence, very efficient when compared to multislice methods for simulating ensembles of crystals with large sizes and complex morphologies. The 3D models used as input for the calculations were obtained either numerically or using electron tomography. The single slice approach relies on slicing the shape factor of the crystal at a distance in reciprocal space given by the effective deviation parameter. It provides combined real and reciprocal space information that is not available from the analytical solutions provided for instance by Kormska and Neumann [14], and the *column approximation* is not necessary. In some of the experiments, it has been found that when compared with the classic Howie-Whelan equation and the column approximation, the single slice approach provides simulated images that match better the experiment (including weak-beam imaging).

The framework was validated comparing simulations with DF TEM images of real samples of MgO and ZrO_2 nanocrystals larger than 100 nm, and with DF TEM images of thin layers of CeO_2. A better accuracy of the simulations is expected by increasing the number of pixels used for modelling the shape. In this way, the slicing in Fourier space can be done with a finer step.

The fine contrast features and *Pendellosung* fringes observed in the experiments could be replicated even when the crystals were not in two-beam conditions. The two-beam condition of diffraction does not exist, it is only an useful simplification. Our experiments suggests that the total intensity of a diffracted beam will decrease or increase depending on the number of active reflections, but the fine structure of the intensity is mostly affected by the shape of the crystal (and the deviation parameter). The MgO crystals studied in this work have shapes with high symmetry hence, the scattered beams will display similar fine structures. The accuracy of the method has been evaluated also on an experimental tilt series of DF TEM images of MgO crystals and it has been used to estimate the value of the extinction distance ξ_{220} of MgO and a normal absorption coefficient lower than expected, $\xi_o' < 10\ \xi_{220}$.

It has been defined a generalized shape function called '*g*-shape function' (Eq. (28)) that is in general different for each reciprocal spot and that it can be used to simulate two-beam electron diffraction by a crystal with defects within the single slice framework. Basic contrast features of dislocations, stacking faults, pores and precipitates were reproduced correctly, including interference fringes at the intersection of planar defects.

The single slice approach presented here can be used to simulate the fine structures of diffracted spots without and with precession (Eq. (15)), and it has been applied to show that even for perfect (undistorted) crystals, the diffracted peaks positions (the absolute maxima) can be shifted, and can have asymmetric distorted shapes with intense subsidiary maxima. Nonetheless, by precessing the beam using PED, most of the distortions of the peaks can be minimised and the spots can be used more reliably for metrological applications, such as for the measurement of crystal size from the peak width or for calibrations. Also, the single slice approach could be applied for simulating X-ray diffraction because the intensity of a diffracted X-ray beam is formally equivalent to the Eq. (1).

Acknowledgments

L. Cervera Gontard acknowledges funding from UCA, through its Support to High Productivity Groups Program. Financial support from the Junta de Andalucía (FQM334) and from the program 'Contratos de acceso al Sistema Español de Ciencia, Tecnología e Innovación' (ASECTI) is acknowledged. A. Barroso-Bogeat thanks support from the "Juan de la Cierva-Formación" Fellowship Program of MINECO (FJCI-2015-25999). Funding from FEDER/MINECO Project Ref. MAT2017-87579-R is also acknowledged.

Appendix

The *Central Slice Theorem* is widely applied for tomographic reconstruction. The theorem states that the projection of a real function in a direction z corresponds to a central section through the Fourier space in the q_x, q_y plane that crosses the origin ($q_z = 0$).

$$D(q_x, q_y, q_z = 0) = \iint \left[\int D(x, y, z)dz \right] e^{(-2\pi i(q_x x + q_y y)} dxdy = \iint z(x, y)\, e^{(-2\pi i(q_x x + q_y y)} dxdy$$

and

$$z(x, y) = |\mathcal{F}T^{-1}\{D(q_x, q_y, q_z = 0)\}| \equiv |\mathcal{F}T^{-1}\{D(0)\}|$$

In terms of the shape factor, given a three-dimensional object $D(r) = D(x, y, z)$ the projected thickness $z(x, y)$ along the direction z it is just the modulus of the inverse Fourier Transform of a central slice of the complex shape factor (with $q_z \equiv s_g = 0$).

MATLAB CODE:

```
%1. PARAMETERS;
clear all; s = 3; %slice number. Change this value to change sg; lambda = 0.00251; % wavelenght of the electron at 200 keV;
ic = 0.007228; %interaction constant at 200 kV; Vg = 6.688; %Fourier coefficient Vg of electrostatic potential for MgO (220); ed = pi/
(ic*Vg); %extinction distance; K = (pi / (lambda*ed))^2; factor = 5; na = factor * ed; %normal absorption; %Angle in degrees out of the
zone axis; angle = -5; %Initialization of the simulation volume D of 128 × 128 × 128 voxels; dm = 128; D = double(zeros(dm,dm,dm));
%2. CREATING THE 3D MODEL SHOWN IN FIGURE 6b;
for x = 1:dm-1
for y = 1:dm-1
for z = 1:dm-1
if abs(7-y+dm/2)+abs(10+z-dm/2) < =9 && abs(10+x-dm/2) < = 9;D(x,y,z) = 1; end
if abs(-6-y+dm/2)+abs(z-dm/2) < =12 && abs(25+x-dm/2) < = 9;D(x,y,z) = 1; end
if abs(-28-y+dm/2)+abs(25+z-dm/2) < =28.5 && abs(-11+x-dm/2) < = 18;D(x,y,z) = 1; end
if abs(21-y+dm/2)+abs(-16+z-dm/2) < =36 && abs(-18+x-dm/2) < = 24;D(x,y,z) = 1; end
end
end
end
%3. ROTATION OF THE MODEL AND DISPLAY;
%The shape function is rotated around the x-axis;
for sl = 1:size(D,2)
IM(:,:) = D(:,sl,:);IMR = imrotate(IM,angle,'crop');D(:,sl,:) = IMR;
end
subplot(1,3,1);[f,v] = isosurface(D,0.9); p = patch('Faces',f,'Vertices',v); set(p,'FaceColor',[1 0.5 0.2]','EdgeColor','none'); alpha(0.9);
daspect([1,1,1]); camlight(150, 40); lighting gouraud; grid on; xlabel('x (nm)'); ylabel('y (nm)'); zlabel('z (nm)'); title('3D shape
function D(x,y,z)','Fontsize',12); set(gca,'fontsize',12); axis([dm/2-60 dm/2+60 dm/2-60 dm/2+60 dm/2-60 dm/2+60]); view([0, -
90]);
%4. SLICING THE 3D FT;
%3D Fourier transform of the shape function Dq;Dq = fftn(D);Dq = fftshift(Dq);
%Slice number referenced to the central slice of the reciprocal volume; sg = dm/2 + 1 + s;
%2D slice of the shape transform; slice(:,:) = Dq(:,:,sg);
%5. SIMULATED DIFFRACTED BEAM AT THE FOCAL PLANE;
%Image of diffracted spot at the focal plane (intensity);FP = K * abs(slice).^2;
%Normalization to 1;FP = FP / max(max(FP));
subplot(1,3,2);imshow(mat2gray(FP),[]);xlabel('q_{x} (nm^{-1})'); ylabel('q_{y} (nm^{-1})'); colormap('gray');
colorbar; title(['I_{g}(qx,qy)=|\phi_{g}|^{2} Focal plane, s_{g}= ' num2str(s)],'Fontsize',12); box on; axis square;
%6. SIMULATED DIFFRACTED BEAM AT THE IMAGE PLANE;
%2D slice of the shape transform; slice(:,:) = Dq(:,:,sg);
% Modulus squared of inverse FT of slice of the shape factor;Ig = K * abs(ifft2(slice)) .^2;
% Thickness; z(x,y) zmap = abs(ifft2(Dq(:,:,dm/2)));
% DFTEM image at the image plane (intensity);Ig = Ig .* exp(-2*pi*zmap/na);
%Normalization to 1;Ig = Ig / max(max(Ig));
subplot(1,3,3); imagesc(0:dm,0:dm,Ig, [0 1]); xlabel('x (nm)'); ylabel('y (nm)'); colormap('gray'); colorbar; title(['I_{g}(x,y)
=|\phi_{g}|^{2} DFTEM, s_{g}= ' num2str(s)],'Fontsize',12); box on; axis square;
```

References

[1] P.B. Hirsch, A. Howie, R.B. Nicholson, D.W. Pashley, M. Whelan, Electron Microscopy of Thin Crystals, Butterworths, London, 1965.

[2] M. De Graef, Introduction to Conventional Transmission Electron Microscopy, Cambridge University Press, 2003.

[3] L. Reimer, Transmission Electron Microscopy: Physics of Image Formation and Microanalysis 36 Springer, 2013.

[4] R. Rasmussen, C.B. Carter, A computer program for many-beam image simulation of amplitude-contrast images, Microscopy Res. Tech. 18 (4) (1991) 429–436.

[5] E.J. Kirkland, Advanced Computing in Electron Microscopy, Springer Science & Business Media, 2010.

[6] P.G. Self, M.A. O'keefe, P.R. Buseck, A.E.C. Spargo, Practical computation of amplitudes and phases in electron diffraction, Ultramicroscopy 11 (1) (1983) 35–52.

[7] C.J.D. Hetherington, L.-Y.S. Chang, S. Haigh, P.D. Nellist, L.C. Gontard, R.E. Dunin-Borkowski, A.I. Kirkland, High-resolution TEM and the application of direct and indirect aberration correction, Microscopy Microanal. 14 (1) (2008) 60–67.

[8] A. Howie, M.J. Whelan, Diffraction contrast of electron microscope images of crystal lattice defects. II. The development of a dynamical theory, Proc. R. Soc.

Lond. A 263 (1313) (1961) 217–237.
[9] A. Howie, Z.S. Basinski, Approximations of the dynamical theory of diffraction contrast, Philos. Mag. 17 (1968) 1039–1063.
[10] A. Howie, H. Sworn, Column approximation effects in high resolution electron microscopy using weak diffracted beams, Philos. Mag. 22 (1970) 861–864.
[11] J.M. Cowley, P. Goodman, A.L.G. Rees, Crystal structure analysis from fine structure in electron diffraction patterns, Acta Crys. 10 (1957) 19–25.
[12] R. De Ridder, J. Van Landuyt, R. Gevers, S. Amelinckx, The fine structure of spots in electron diffraction resulting from the presence of planar interfaces and dislocations. IV. Wedge crystals, Physica Status Solidi 30 (2) (1968) 797–815.
[13] W. Neumann, J. Komrska, H. Hofmeister, J. Heydenreich, Interpretation of the shape of electron diffraction spots from small polyhedral crystals by means of the crystal shape amplitude, Acta Cryst. A44 (1988) 890–897.
[14] J. Komrska, W. Neumann, Crystal shape amplitudes of platonic polyhedra. I. General aspects and the shape amplitudes of the tetrahedron, cube, and octahedron, Physica Status Solidi 150 (1) (1995) 89–111.
[15] R. Dronyak, K.S. Liang, J.S. Tsai, Y.P. Stetsko, T.K. Lee, F.R. Chen, Electron coherent diffraction tomography of a nanocrystal, Appl. Phys. Lett. 96 (22) (2010) 221907.
[16] M.J. Hÿtch, F. Houdellier, F. Hüe, E. Snoeck, Dark-field electron holography for the measurement of geometric phase, Ultramicroscopy 111 (8) (2011) 1328–1337.
[17] C.J. Humphreys, The scattering of fast electrons by crystals, Rep. Progr. Phys. 42 (1979) 1827–1883.
[18] R. Vincent, P.A. Midgley, Double conical beam-rocking system for measurement of integrated electron diffraction intensities, Ultramicroscopy 53 (3) (1994) 271–282.
[19] B.D. Forbes BD, A.J. D'Alfonso, S.D. Findlay, D. Van Dyck, J.M. LeBeau, S. Stemmer S, L.J. Allen, Thermal diffuse scattering in transmission electron microscopy, Ultramicroscopy 111 (2011) 1670–1680.
[20] H. Hashimoto, Energy dependence of extinction distance and transmissive power for electron waves in crystals, J. Appl. Phys. 35 (1964) 277.
[21] C.J. Humphreys, P.B. Hirsch, Absorption parameters in electron diffraction theory, Philos. Mag. 18 (151) (1968) 115–122.
[22] Z. Zhou, M.L. Jenkins, S.L. Dudarev, A.P. Sutton, M.A. Kirk, Simulations of weak-beam diffraction contrast images of dislocation loops by the many-beam Howie–Basinski equations, Philos. Mag. 86 (29-31) (2006) 4851–4881.
[23] G.Y. Fan, M.H. Ellisman, Digital imaging in transmission electron microscopy, J. Microscopy 200 (2000) 1–13.
[24] L.C. Gontard, G. Moldovan, R. Carmona-Galán, C. Lin, A.I. Kirkland, Detecting single-electron events in TEM using low-cost electronics and a silicon strip sensor, Ultramicroscopy 63 (2) (2014) 119–130.
[25] G. Honjo, K. Mihama, Fine structure due to refraction effect in electron diffraction pattern of powder sample part II. Multiple structures due to double refraction given by randomly oriented smoke particles of magnesium and cadmium oxide, J. Phys. Soc. Jpn. 9 (2) (1954) 184–198.
[26] F.M. Morales, D. González, J.G. Lozano, R. García, S. Hauguth-Frank, V. Lebedev, V. Cimalla, O. Ambacher, Determination of the composition of InxGa1-xN from strain measurements, Acta Materialia 57 (19) (2009) 5681–5692.
[27] L.C. Gontard, J. Cintas, R.E. Dunin-Borkowski, The benefit of thresholding carbon layers in electron tomographic tilt series by intensity downshifting, J. Microscopy 265 (3) (2016) 298–306.
[28] M. Tinoco, J.J. Sanchez, M.P. Yeste, M. Lopez-Haro, S. Trasobares, A.B. Hungria, P. Bayle-Guillemaud, G. Blanco, J.M. Pintado, J.J. Calvino, Low-Lanthanide-content CeO_2/MgO catalysts with outstandingly stable Oxygen storage capacities: an in-depth structural characterization by advanced STEM techniques, Chem. Cat. Chem. 7 (2015) 3763–3778.